Simulation of the Transonic Truss-Braced Wing High-Lift Configuration at Mach 0.20 using USM3D-Mixed Element Solver

Tausif Jamal*, Seth Kelly†, Craig Hunter‡, William Milholen§, T.J. Wignall¶, and Steven Krist#

NASA Langley Research Center, Hampton, VA, 23681, USA

Numerical simulations for the high-lift configuration of the Transonic Truss-Braced Wing (TTBW) are carried out using the USM3D-ME flow solver with unsteady Reynolds-averaged Navier-Stokes (URANS) turbulence models at a Mach Number of 0.20 and a chord Reynolds number of 0.98×10^6. Results from numerical simulations are compared against a wind-tunnel experiment carried out in the 14-by 22-Foot Subsonic Wind Tunnel at the NASA Langley Research Center. Results indicate that the simulations are in close agreement with experimental data for low angles of attack. However, significant discrepancies between experiment and simulations are observed at high angles of attack near the stall region. The largest deviation from experimental data occurs outboard of the strut-wing intersection, where flow separation is observed. It is concluded that although industry-standard RANS models are able to predict flow features associated with a high-lift configuration with some accuracy, improved turbulence models with scale-resolving capabilities should be considered, especially in the stall and post-stall region.

Nomenclature

α	=	Angle of attack, degrees
BC	=	Boundary Condition
C_L	=	Lift Coefficient
C_D	=	Drag Coefficient
C_p	=	Pressure Coefficient
C_f	=	Magnitude of Skin Friction Coefficient
CFD	=	Computational Fluid Dynamics
CTU	=	Convective Time Unit
CRM	=	Common Research Model
HL	=	High Lift
HRL	=	Hybrid RANS-LES
LES	=	Large Eddy Simulation
M_∞	=	Freestream Mach number
ME	=	Mixed Element
NASA	=	National Aeronautics and Space Administration
RANS	=	Reynolds-averaged Navier-Stokes
SA	=	Spalart-Allmaras baseline turbulence model
SA-Neg	=	Negative version of Spalart-Allmaras turbulence model
SST k-ω	=	Shear Stress-Transport *k-ω* turbulence model
TTBW	=	Transonic Truss-Braced Wing
R	=	Rotation Correction
RC	=	Rotation and Curvature Correction
SUGAR	=	Subsonic Ultra-Green Aircraft Research
QCR	=	Quadratic Constitutive Relation
URANS	=	Unsteady Reynolds-averaged Navier-Stokes

* Configuration Aerodynamics Branch, tausif.jamal@nasa.gov.
† Configuration Aerodynamics Branch, AIAA Member, seth.w.kelly@nasa.gov.
‡ Configuration Aerodynamics Branch, craig.hunter@nasa.gov.
§ Configuration Aerodynamics Branch, AIAA Senior Member, william.e.milholen@nasa.gov.
¶ Configuration Aerodynamics Branch, thomas.j.wignall@nasa.gov.
# Configuration Aerodynamics Branch, AIAA Senior Member, steven.e.krist@nasa.gov.

I. Introduction

The prediction of aerodynamic performance of high-lift configurations is challenging for even the most advanced turbulence models. Studies [1,2] have shown that Computational Fluid Dynamics (CFD) codes and turbulence models can be inconsistent for high-lift configurations and often predict inaccurate lift, drag, and pitching moment at high angles of attack. The inclusion of flaps, slats, and spoilers provide challenging conditions for modern computational tools to accurately resolve the flow field associated with high-lift configurations. For example, the flow field around high-lift configurations often contains adverse pressure gradients, vortex shedding, laminar-to-turbulent transition, compressibility effects, rotation and curvature effects, and regions of spatially and temporally varying turbulence intensities. Strong jets can also flow between the components, leading to flow features such as wake bursting [3].

Pandya et al. [4] evaluated the performance of the Spalart-Allmaras (SA) [5] and the Shear-Stress Transport (SST) k-ω [6] models for the generic high-lift NASA Trapezoidal (Trap) Wing Configuration. The NASA Trap wing consists of a three-element wing with a full-span slat and flap combination. Two different slat and flap configurations were simulated using USM3D [7-10] and results were compared to experimental data from the 14- by 22-Foot Subsonic Wind Tunnel at the NASA Langley Research Center. Results indicated that the SA model tracked lift and drag coefficient closely. Although disagreement from experiments for pitching moment was observed for both models, the SA model consistently produced improved results when compared to the SST k-ω model. Surface pressure data indicated that disagreements between numerical simulations and experiments grew for both models towards the outboard section of the wing. Overall, it was concluded that the SA model provides significantly improved predictive capability when compared to the SST k-ω model for this type of flow and configuration.

Numerical simulations for the landing configuration of the NASA High Lift Common Research Model (CRM-HL) [11] and the JAXA Standard Model were carried out by Coder et al. [12] using Overflow and LAVA. The CRM-HL was developed by Boeing as a representative example for a high-lift configuration aircraft for the CRM. Simulations were carried out for $M_\infty = 0.20$ at $\alpha = 8°$ and 16°. The authors concluded that using a model with Quadratic Constitutive Relation (QCR) such as the SA-QCR-2000 model [13] provided consistent results for the various configurations. Additionally, the authors also observed that laminar-to-turbulent transition was non-negligible for these types of configurations.

Numerical simulations for the CRM-HL model were also carried out by Bozeman et al. [14] using the USM3D-ME [15-19] solver. Numerical solutions were obtained using the SA-Neg [20] and SA-Neg-RC-QCR [13,20,21] models to study the effects of flap deflection, grid refinement, and angle of attack sweep. Results were compared to experimental data obtained from the QinetiQ low-speed wind tunnel [22]. The authors observed that both models underpredicted pressure on the suction side of the airfoil. Consequently, both models underpredicted lift coefficient while overpredicting drag coefficient. The disagreement grew as angle of attack was increased. Interestingly, the SA-Neg model without any corrections tended to capture the flow behavior more accurately than the SA-Neg-RC-QCR model, which is considered to be a best practice Reynolds-averaged Navier Stokes (RANS) model for these types of flows.

From the examples provided above, it is clear that prediction of high-lift configurations is an area of ongoing research. Most research using RANS models have found them to be comparatively less reliable than scale-resolving methods. These challenges are further exacerbated with the addition of complex fairings, brackets, and wing-strut designs in an attempt at improving aerodynamic efficiency while incorporating high-aspect ratio wings. Since induced drag is inversely proportional to the aspect ratio of a wing, high-aspect ratio wings have the potential to increase operating efficiency significantly. However, a major drawback of high-aspect ratio wings is the need to have root structures that are strong enough to withstand the bending moment associated with these types of wings. A solution this problem is to utilize a truss-like structure to provide support without incurring the penalty of adding significant weight. One such concept is the Transonic Truss-Braced Wing (TTBW).

In 2008, the NASA/Boeing Subsonic Ultra-Green Aircraft Research (SUGAR) program was initiated to conduct research into advanced subsonic air-transport concepts. The aim of the project was to meet NASA-defined system-level metrics and goals such as reduced acoustic signature and increased aerodynamic efficiency for a 2030-2035 entry into service. Based on initial estimates, the SUGAR TTBW vehicle concept is expected to reduce fuel consumption

by as much as 60% when compared to a single aisle commercial transport such as the Boeing 737-800. The SUGAR TTBW achieves this by utilizing high-aspect ratio wings that are supported with a truss. For comparison, the aspect ratio of the SUGAR TTBW wing is approximately 19.55, which is almost an 85% increase compared to a traditional cantilever aircraft such as the Boeing 777, which is reported to have an aspect ratio of approximately 11. This configuration enables a significant decrease in aerodynamic drag in addition to providing the option for larger high-bypass engine integration. Figure 1 shows the SUGAR TTBW Mach 0.80 concept with various components.

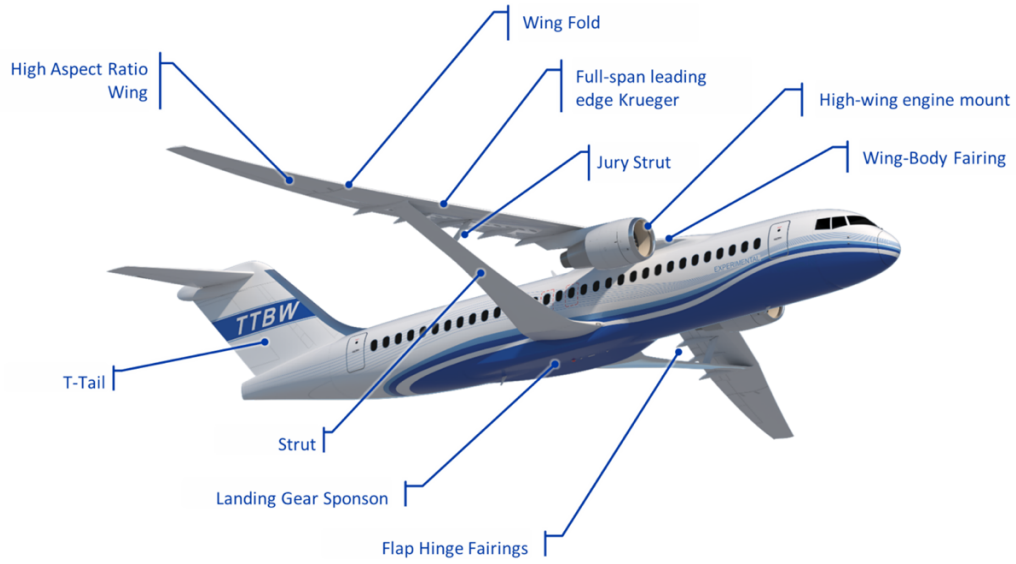

Figure 1. SUGAR TTBW Concept Mach 0.80 Configuration [23].

Since the inception of the NASA/Boeing SUGAR TTBW concept, there have been several changes to the design based on mission requirements and improved efficiency targets. This paper focuses on the Mach 0.80 version in Phase IV of the project. This version differs from its predecessor, Mach 0.745 version, in wing sweep, airfoil thickness, and adjusted center of gravity. Some of the main improvements in this modification includes reduced drag and enhanced structural strength of the wing-strut system [23].

Several key numerical studies have been conducted in the last decade to support the development of the SUGAR concept, supported by experimental measurements. Maldonado et al. [24] conducted simulations of the SUGAR TTBW Mach 0.745 version using USM3D [7-10] and LAVA [25] CFD codes for configurations tested at the 11- by 11-foot Unitary Plan Wind Tunnel at NASA Ames. Although both codes were in agreement with each other for free air simulations, large discrepancies were observed when the results were compared to the experimental data. Lift and drag coefficients were overpredicted by both codes with even larger disagreements arising for pitching moment predictions. Additional simulations representing the model within the wind tunnel were performed using porous media to simulate the effects of the tunnel walls more accurately. Although minimal improvements were observed, the new setup represented the non-linear region in the lift coefficient (C_L) curve slightly better.

Viken et al. [26] performed free-air simulations for the Mach 0.80 version using USM3D [7-10], USM3D-ME [15-19], and LAVA [25] for different wing, body, nacelle/pylon, strut, flap, hinge-fairing, and vertical tail configurations. The USM3D and USM3D-ME codes used SA [5,20] and SA-QCR [13] turbulence models, while LAVA used only the SA-QCR-RC [13,20,21] model. All three codes were in agreement with each other. Major differences were only observed for at high angles of attack. Additionally, some differences were also observed for pitching moment predictions due to the differences in predicted normal-shock location. For the wind tunnel computations, LAVA predicted slightly higher drag while USM3D-ME predicted higher drag when the nacelle pylon and flap hinge fairings were added. Spanwise pressure distribution data correlated well with experiments except for the region near the strut-wing channel.

The unsteady nature of the flow associated with these types of configurations, in addition to the complex interactions caused by leading-edge slats, flaps, flap-track fairing, and brackets, result in an environment that is highly unsuitable for RANS turbulence models. Although recently there has been some success using Hybrid RANS-LES (HRL) methods such as DES [27], DDES [28], and DHRL [29,30] for complex turbulent flows, the low computational

overhead associated with RANS models still makes them an attractive choice during initial design investigations. Hence, it is important to evaluate the performance of the industry-standard RANS turbulence models for this type of configuration. Although there are advanced second-moment closure models capable of predicting Reynolds-stress anisotropy such as algebraic Reynolds-stress models [32,33], it is important to completely understand the shortcomings and the strengths of the linear-eddy viscosity models first.

The main objective of the current study is to evaluate the performance of industry-standard turbulence models i.e., the SA [5,20] model and its variants using the cell-centered finite-volume solver USM3D-ME [15-19] for the SUGAR TTBW high-lift configuration. Performance of the selected models is evaluated against experimentally obtained data from 14- by 22-foot Subsonic Wind Tunnel at NASA Langley Research Center for integrated forces and pitching moment.

II. Turbulence Modeling Approaches

Turbulent flows are often accompanied by the presence of complex flow features such as wakes, vortices, and regions of boundary separation. Additionally, the complex interaction associated with different scales of motion and regions of spatially and temporally evolving turbulence makes prediction of these types of flows a daunting task. Modern turbulence modeling approaches can be broadly categorized into three different classes: RANS, Large Eddy Simulation, and Direct Numerical Simulation. RANS solves only the ensemble or time-averaged equations of fluid motion and models all scales of fluctuating motion; LES solves the Navier-Stokes equations for some scales and models the others, while DNS explicitly solves the Navier-Stokes equations for all scales of motion. The theoretical accuracy of each of these methods is directly proportional to the range of resolved scales, as is the computational expense. Hence, DNS is the most accurate numerical method available today, but it is prohibitively expensive for complex engineering problems. Even LES can be too expensive for engineering purposes based on the resolution of the method, requiring several days or even weeks of runtime on typical High-Performance Computing architectures. Because of this, RANS turbulence models are the most commonly used numerical models in applied CFD. Since their inception almost five decades ago, RANS models have been validated for an extensive number of test cases and practical engineering problems. RANS models perform relatively well for attached wall-bounded problems and are computationally inexpensive, which makes them the natural choice for most engineering applications.

For the current study, variants of the Spalart-Allmaras (SA) RANS turbulence model are used. The SA model [5] is a one-equation linear eddy-viscosity model that has been extensively validated and verified for numerous applications specifically in the aerospace industry. The model has been shown to perform well in boundary layers and in regions of adverse pressure gradients. The SA model solves a transport equation for the modified viscosity which is used to close the RANS equations. Apart from the baseline SA model, the SA-Neg [20] model is also used in this study. The SA-Neg model addresses some of the shortcomings of the baseline SA model where the model produces non-physical results in the presence of under-resolved grids, the edge of boundary layers, wakes, and when the modified vorticity becomes negative. To address this issue, the SA-Neg model was proposed by Allmaras et al. [20]. When the modified viscosity ($\tilde{\upsilon}$) < 0, a modified equation is solved, and the turbulent viscosity (υ_t) is set to zero. In this case, the modified viscosity is treated as a passive scalar. Also evaluated is the Quadratic Constitutive Relation (QCR) variant of the SA-Neg model. The traditional linear eddy viscosity approach adopted in the development of the baseline SA models does not reproduce complex flow physics such as streamline curvature and Reynolds stress anisotropy. This was highlighted by problems such as corner flow in a duct [34] and NASA Juncture Flow [35-37]. The SA-QCR2000 [13] model was developed to address these issues. The SA-QCR2000 model introduces terms that are quadratic in the mean vorticity and strain tensors to represent the Reynolds stress tensor. Additional variants of the QCR model exist in the form of QCR2013 [38] and QCR2020 [39] however, they are not currently available for use in the current version of USM3D-ME. Also, the QCR2000 model is more widely used and implemented in the industry. It must be noted that in this paper from this section onwards, the QCR2000 model is sometimes referred only as QCR. Other approaches to representing the anisotropic part of the Reynolds stress tensor have also been presented by Rodi [40] and Wallin et al. [33] for two-equation models. For additional details, readers are referred to [41-43]. Finally, to account for system rotation and streamline curvature effects, rotation correction proposed by Dacles-Mariani et.al [44-45] and the rotation-curvature correction proposed by Shur et al. [21] are also evaluated.

III. Experimental Setup

Wind tunnel tests for the SUGAR TTBW high-lift configuration were performed at the 14- by 22-Foot Subsonic Wind Tunnel at NASA Langley Research Center, a closed circuit single-return, fan driven, atmospheric wind tunnel. The tunnel's main drive is a 12,000 hp solid state converter with synchronous motor. The test section size is 14.5 ft in height, 21.75 ft in width, and 50 ft in length [46]. The maximum speed of the facility is 235 miles per hour, or 348

feet per second, with a maximum unit Reynolds number of 2.2 x 10^6 per foot and a dynamic pressure range of 0-144 pounds per square foot psf. The tunnel has a set of flow control vanes to maintain close control of the speed for low-speed testing and a boundary layer removal system that can be used to reduce the thickness of the boundary layer on the tunnel floor during the testing of floor mounted semi-span models. Figure 2 shows an aerial view of the 14- by 22-Foot Subsonic Wind Tunnel at NASA Langley Research Center along with the tunnel circuit layout.

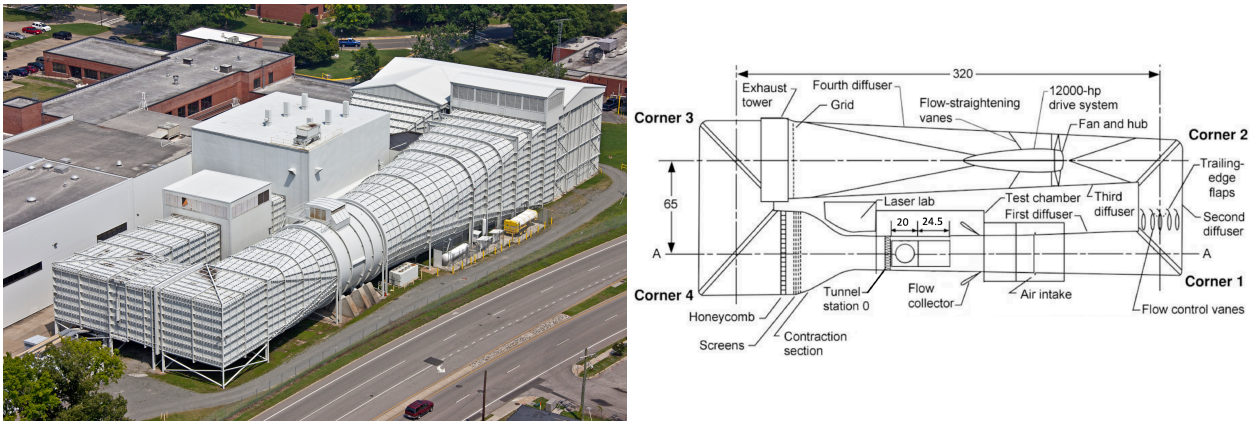

(a) Aerial view [Photo: NASA]. (b) Tunnel circuit layout.

Figure 2. 14- by 22-Foot Subsonic Wind Tunnel – NASA Langley Research Center.

The wind tunnel model is a full-span 8% scale representation of the SUGAR TTBW Mach 0.80 vehicle. The model includes various control surface deflections for investigation into different vehicle configurations such as cruise, takeoff, and landing. Additionally, there is the capability for the model to be mounted to the tunnel support system via a bottom mount (ventral) or top mount (dorsal).

The primary instrumentation devices used for comparison include 9 chordwise surface pressure orifice rows on the wing and 4 chordwise rows along the flaps but no instrumentation was included on the Krueger flaps. Due to the small wing thickness, the chordwise pressure rows were split between the left and right sides of the model. The strut included instrumentation to measure pressure, however this study is only limited to the main wing and flap. The chordwise surface pressure orifice rows on the wing and wing flap are illustrated in Fig. 3.

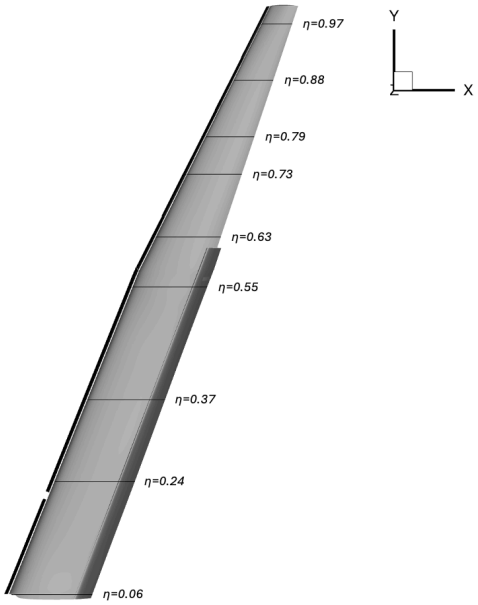

Figure 3. Pressure taps on the wing surface (strut not shown).

IV. Computational Geometry

For the current study, the high-lift configuration of the SUGAR TTBW is considered, which consists of the wing and wing fairing, fuselage body and sponson, wing supporting strut, nacelle and pylon, flap hinge fairings, extended flaps, Krueger flaps, horizontal tail, and vertical tail. For this study, the half-span geometry (see Fig.4) is considered in order to reduce computational overhead.

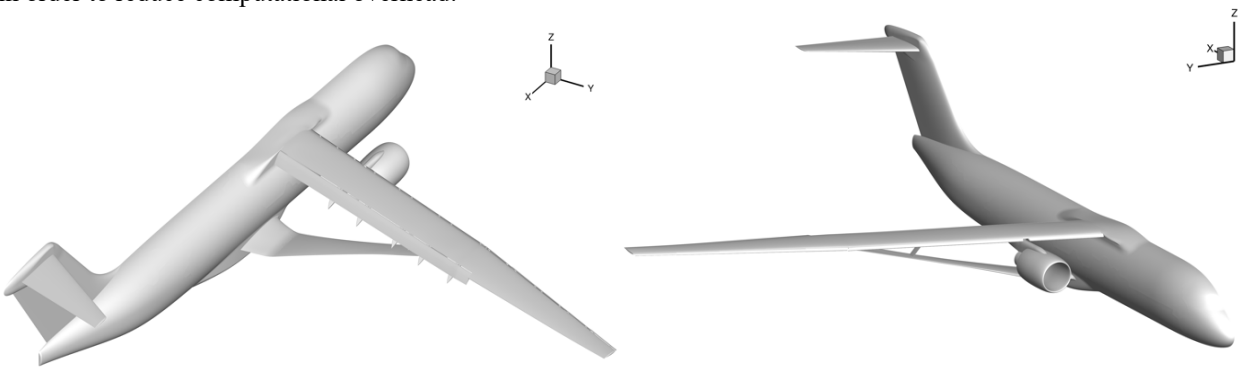

(a) Oblique views of the SUGAR TTBW half-span geometry.

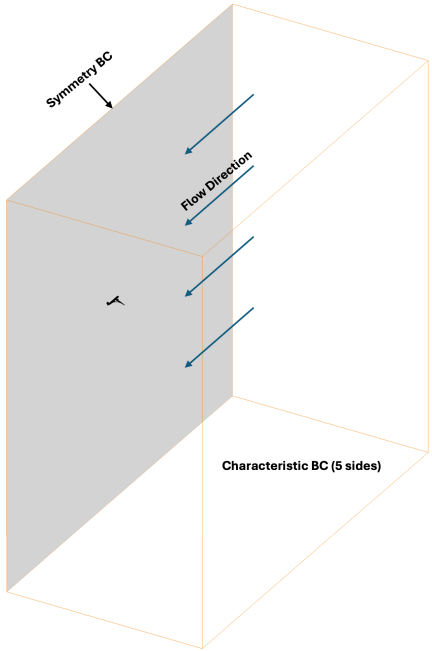

(b) Computational domain.

Figure 4. Visual representation of the SUGAR TTBW half-span geometry and computational domain.

V. Computational Mesh

Three versions of the SUGAR TTBW mesh were generated using HeldenMesh [48]. The first cell height was kept at a y+ value of 1 (y+ of 0.5 at the cell center) for all three versions, while the refinement factor and source growth rates were adjusted. The three resulting grids contained 48.78 million, 96.05 million, and 211.79 million cells. Table 1 highlights the different meshes and their refinement factors.

Figures 5-8 compare the three meshes utilized for the grid convergence study. One of the most notable differences between them can be observed in the growth rate and extent of the prism boundary layer cells. As the mesh is refined, the viscous layers grow up to the local cell size of the advancing front and the handoff between the boundary layer and the outer cells takes place. With smaller outer cells, the handoff occurs sooner, closer to the wall. Additionally,

increased grid density is observed in the vicinity of the Krueger flap brackets, and leading and trailing edges in order to resolve turbulent structures associated with the highly unsteady wakes generated for high-lift configurations.

Table 1. SUGAR TTBW mesh setup.

Grid	Refinement Factor	Source Growth	Wall y^+	Cells
Coarse	1.4	0.28	0.5	48.78 x 10^6
Nominal	1	0.20	0.5	96.05 x 10^6
Fine	0.7	0.14	0.5	211.79 x 10^6

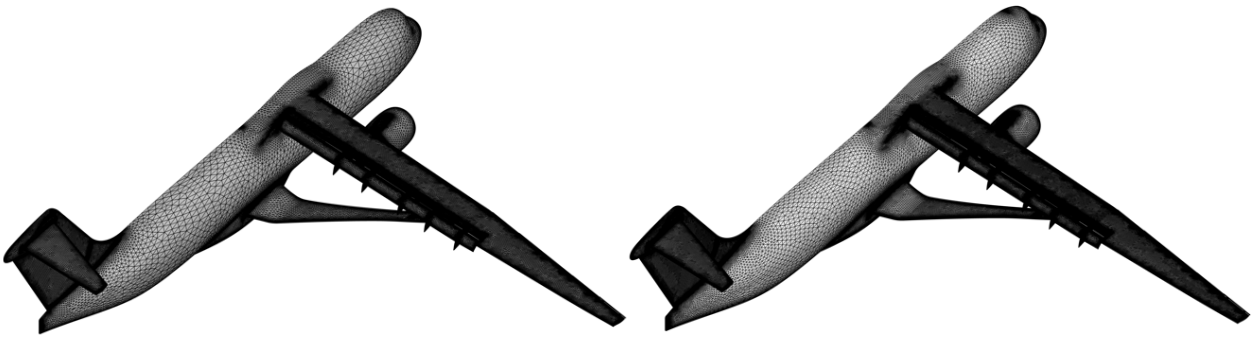

(a) Mesh density for the coarse grid.

(b) Mesh density for the nominal grid.

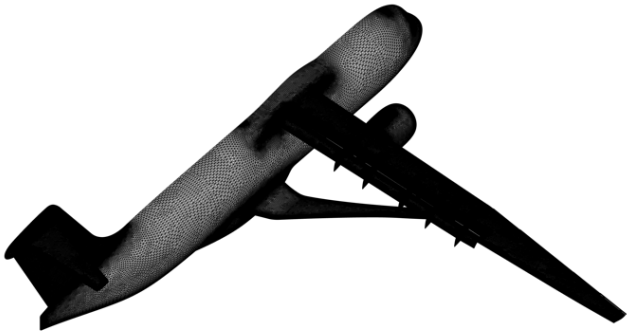

(c) Mesh density for the fine grid.

Figure 5. Comparison of mesh density on half-span surface geometry for all the grids considered in the grid convergence study.

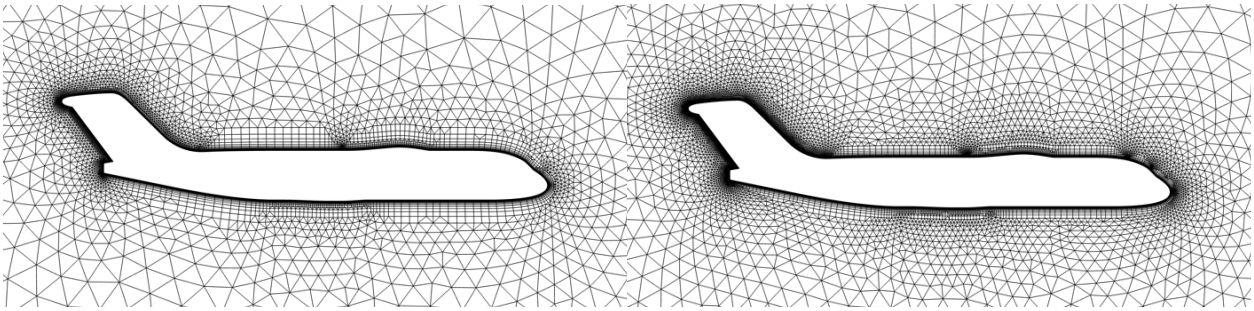

(a) Mesh density for the coarse grid.

(b) Mesh density for the nominal grid.

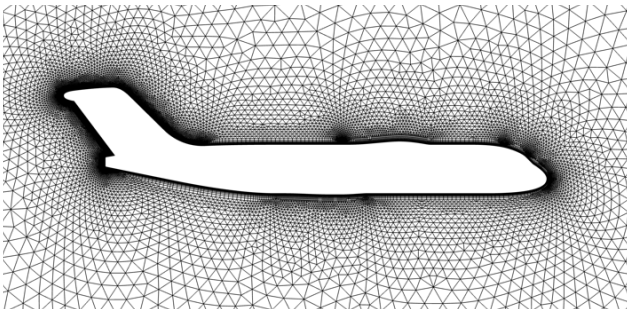

(c) Mesh density for the fine grid.

Figure 6. Comparison of mesh density on the reflection plane highlighting the wall-normal cell growth rate for all the grids considered in the grid convergence study.

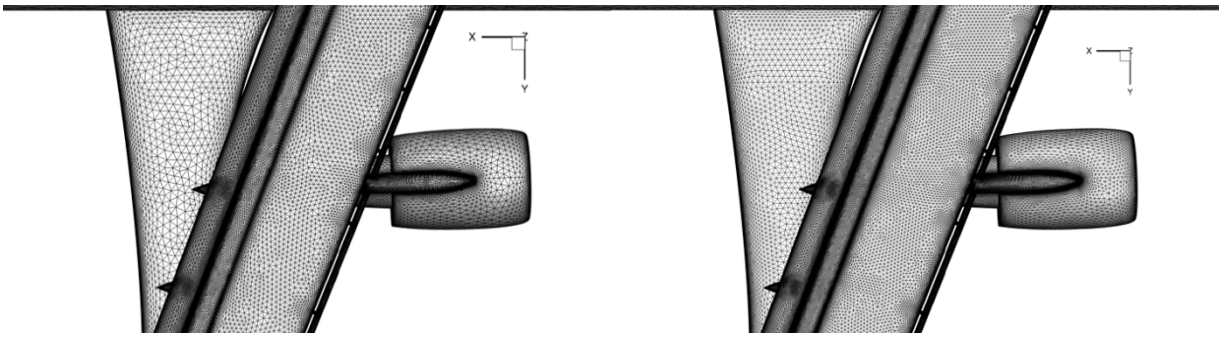

(a) Mesh distribution for coarse grid.

(b) Mesh distribution for nominal grid.

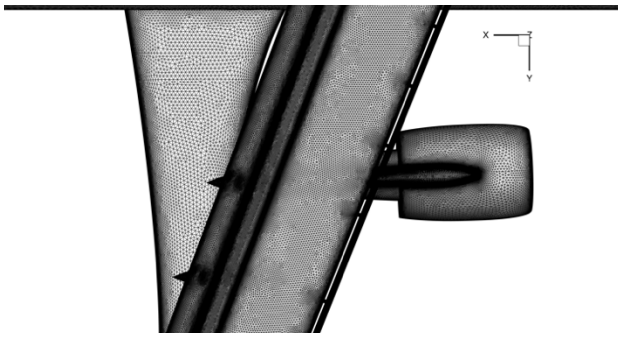

(a) Mesh distribution for fine grid.

Figure 7. Comparison of mesh distribution around the nacelle for all the grids considered in the grid convergence study.

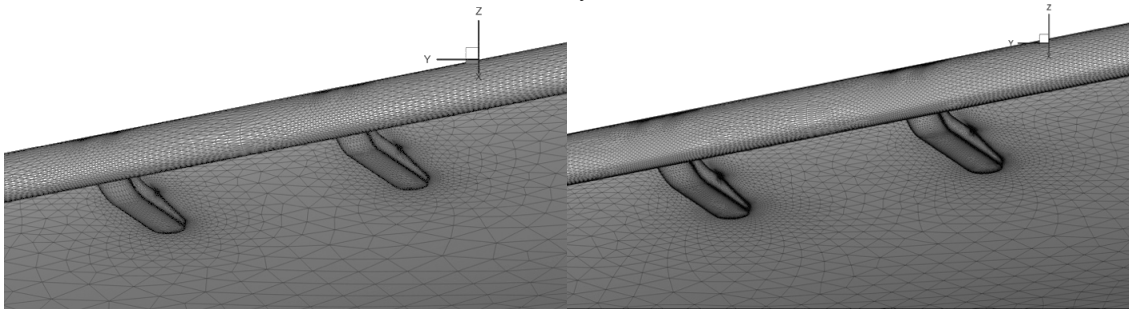

(a) Mesh density for coarse grid.

(b) Mesh density for medium grid.

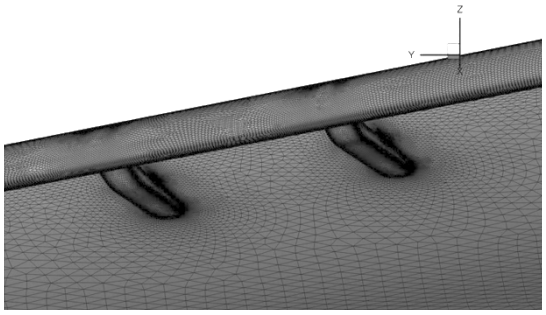

(c) Mesh density for fine grid.

Figure 8. Comparison of the mesh distribution near the Krueger flap brackets for all the grids considered in the grid convergence study.

VI. Numerical Methods

Numerical simulations using URANS models were carried out using the USM3D-ME [15-19] solver. USM3D-ME is a cell-centered, finite volume solver developed at the NASA Langley Research Center. It utilizes unstructured mixed element (ME) grids consisting of tetrahedral cells away from the wall in the freestream regions, while the near-wall boundary layer regions are discretized using prismatic cells. The transition layer between the prisms and tetrahedrons are discretized using pyramid cells. USM3D-ME uses a strong linear solver that significantly increases computational robustness and efficiency called Hierarchical Adaptive Non-Linear Iteration Method [17]. For the current study, the convective terms were discretized with 2nd order spatial accuracy while inviscid flux quantities were computed with Roe's flux-difference-splitting FDS scheme. For each angle of attack, steady-state simulations were first run using local time-stepping and implicit defect-correction schemes. Once steady-state solutions were deemed to be converged, unsteady simulations were carried out with 50 time-steps per convective time unit (CTU) based on $M_\infty = 0.20$ and mean-chord length. Additionally, a maximum of 20 inner iterations per time-step were specified for improved convergence. Table 2 highlights all the different turbulence models and angles of attack considered in the study. Note that the QCR2000 variant is referred to as QCR for all the figures and discussions below.

Table 2. Simulation Run Matrix.

Geometry	α	Turbulence Model
SUGAR TTBW Mach 0.80 High-Lift Configuration	-4°, 8°, 12°, 18°,19°, 20°, 21°, and 22°	SA-Neg-R, SA-Neg-RC, SA-Neg-QCR, SA-Neg-R-QCR, SA-Neg-RC-QCR
	0°, 4°, and 16°	SA-Neg-QCR

VII. Results

A. Mesh Sensitivity and Solution Convergence

Figure 9 (a) compares the predicted lift coefficient (C_L) and the predicted drag coefficient (C_D) for the three grids described earlier to determine mesh sensitivity. Some sensitivity due to grid resolution is observed for the C_L when going from coarse to the nominal grid. Interestingly, in comparisons not presented in this study, the coarse grid provides improved integrated force and pitching moment predictions when compared to finer grids. This is due to the added numerical dissipation associated with the coarse grids, which damp out instabilities and promote flow reattachment in separated zones. Results discussed in this paper correspond to simulations carried out using the nominal grid.

Figure 9 (b) compares the effect of three different time-step sizes or number of time-steps per convective time-unit. Based on the results, it is evident that increasing the number of time-steps per CTU results in minor differences at high angles of attack. Additionally, these minor differences in integrated forces and pitching moments at high angles of attack are insignificant compared to the differences between simulation results and experimental observation. Hence, 50 steps per-CTU was deemed to provide a sufficiently large time-step size for URANS. From past studies it

has been observed that a good approximation for the number of time-steps per CTU for URANS is between 50 and 200.

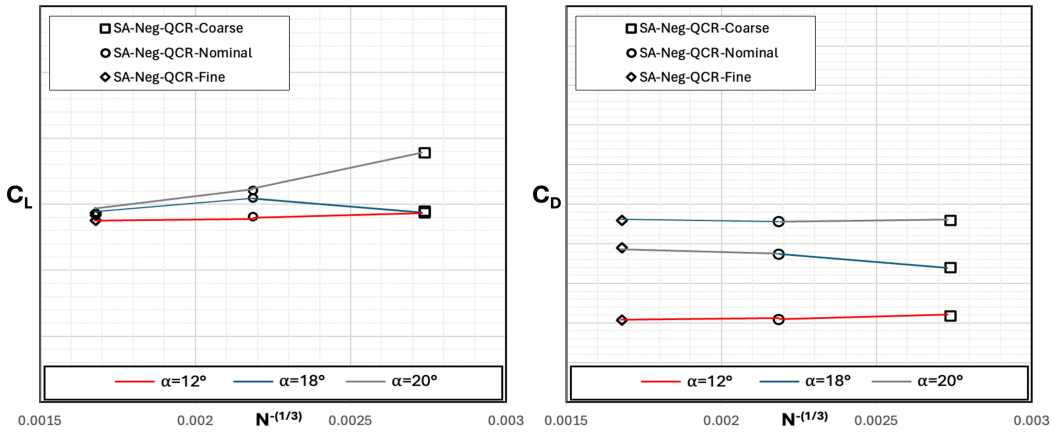

(a) Comparison of predicted integrated forces (C_L and C_D) for different mesh densities.

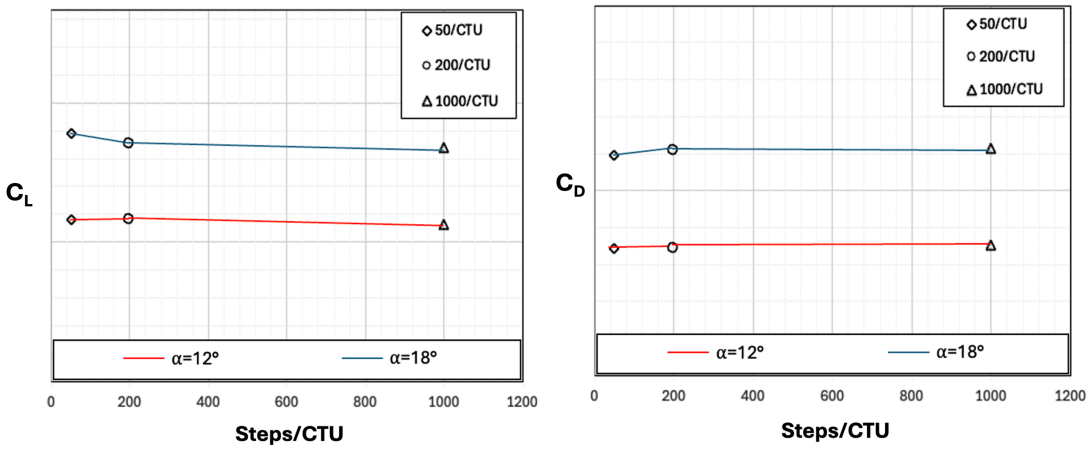

(b) Comparison of predicted integrated forces (C_L and C_D) for different time-step sizes.

Figure 9. Mesh and time-step convergence results.

Figure 10 depicts the histories of root-mean square (RMS) of the residuals of all the turbulence models investigated in this study at different angles of attack. Residuals approach machine-zero during the first 2000 iterations as they are run as steady-state first order (spatial) accurate solutions. Then they are solved using 2nd order spatial accuracy which results in increased residuals that tend to exhibit oscillatory behavior as is expected from an unsteady problem. All the simulations are then solved using 2nd order temporal accuracy which eventually reduce residuals by 3-to-4 orders of magnitude. Once the integrated forces and moments enter limit-cycle behavior, they are then averaged over the last 30 CTU's.

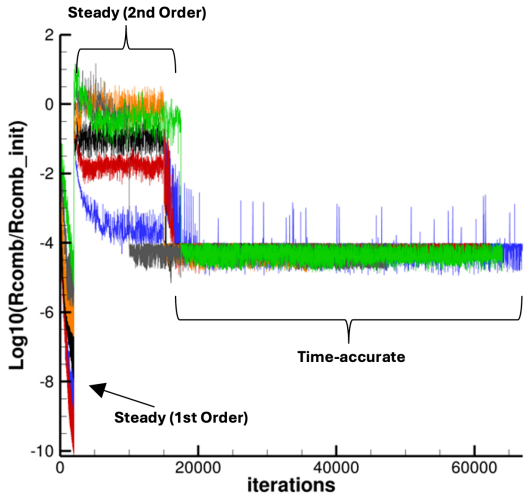

(a) RMS of residuals for SA-Neg-R.

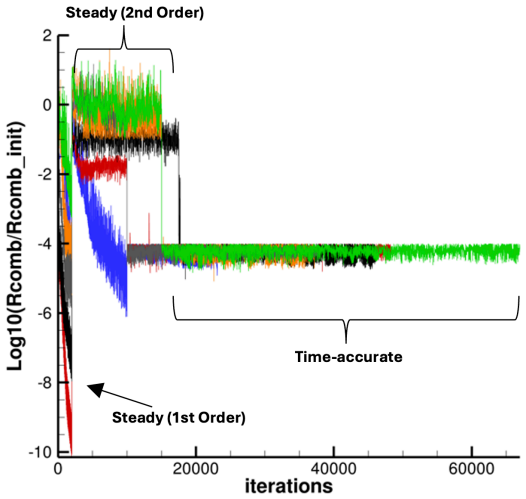

(b) RMS of residuals for SA-Neg-RC.

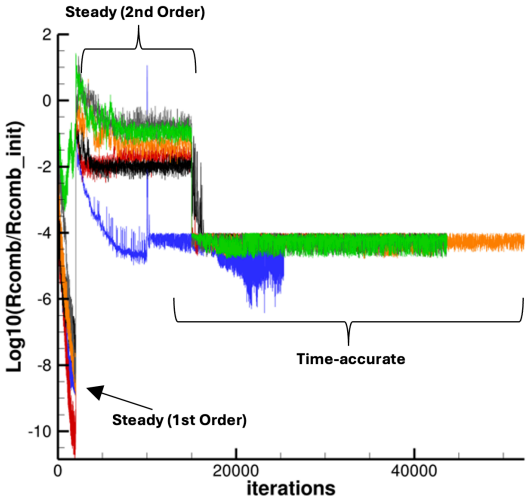

(c) RMS of residuals for SA-Neg-QCR.

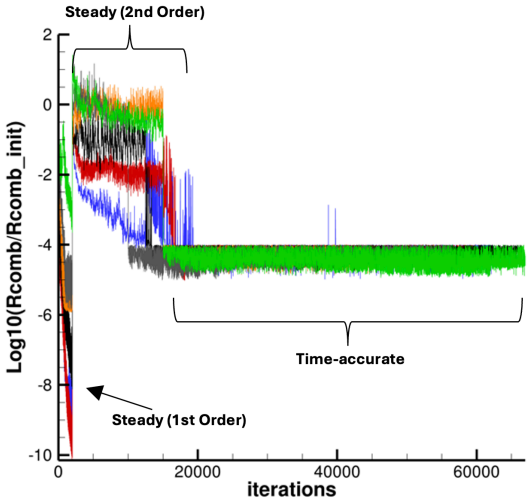

(d) RMS of residuals for SA-Neg-R-QCR.

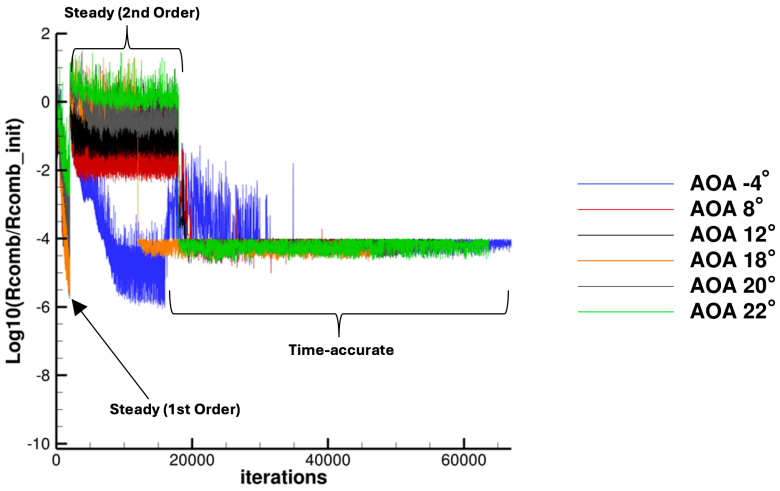

(e) RMS of residuals for SA-Neg-RC-QCR

Figure 10. Comparison of residual convergence.

B. Lift & Drag Coefficient

Figures 11 and 12 compare the C_L ,C_D, drag polar, and C_m obtained from numerical simulations using the SA-Neg-R, SA-Neg-RC, SA-Neg-QCR, SA-Neg-R-QCR, and SA-Neg-RC-QCR models against the experiment carried out at the 14-by 22-Foot Subsonic Wind Tunnel at NASA Langley Research Center. All the models predict lift and drag with relatively high accuracy for the linear region of the lift curve. Although at α = -4° all the models underpredict lift but overpredict drag and pitching moment, most of the linear region of the lift curve is well predicted with all the models accounting for the lift break past α = 12° relatively well. Interestingly, all the models predict early stall between α = 17°-18°. This is primarily due to the prediction of large regions of separated flow on the suction side of the wing that inhibits lift production, which are not present in the experimental data. Post-stall, both the SA-Neg variants' (R and RC) predictions are in best agreement with experimental measurements. Although the post-stall trends are similar to experimental observations, all the models underpredict lift significantly. Similarly, pitching moment is also predicted with relatively high accuracy for α < 15°. Post pitch-break, the SA-Neg-QCR performs the best, while the other model predictions vary significantly. Overall, all the model predictions are in fairly reasonable agreement until stall which is expected as RANS models are known to perform relatively well in the linear region of the lift curve.

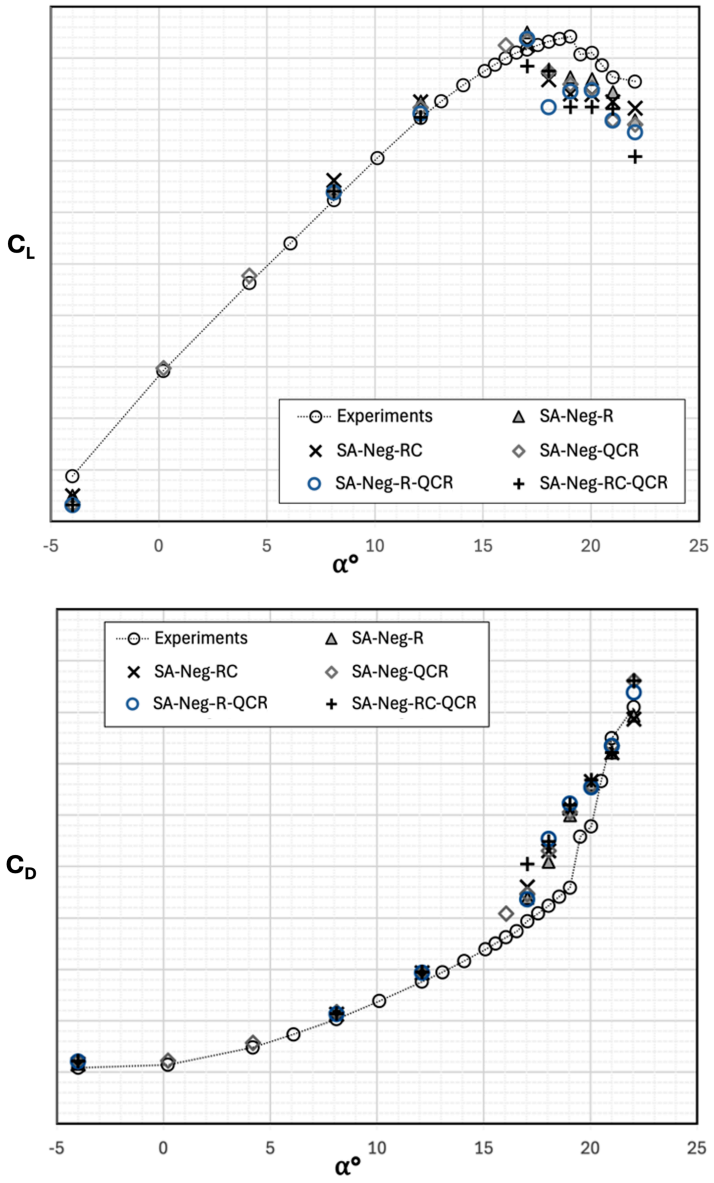

Figure 11. Comparison of the lift coefficient (C_L) and drag coefficient (C_D).

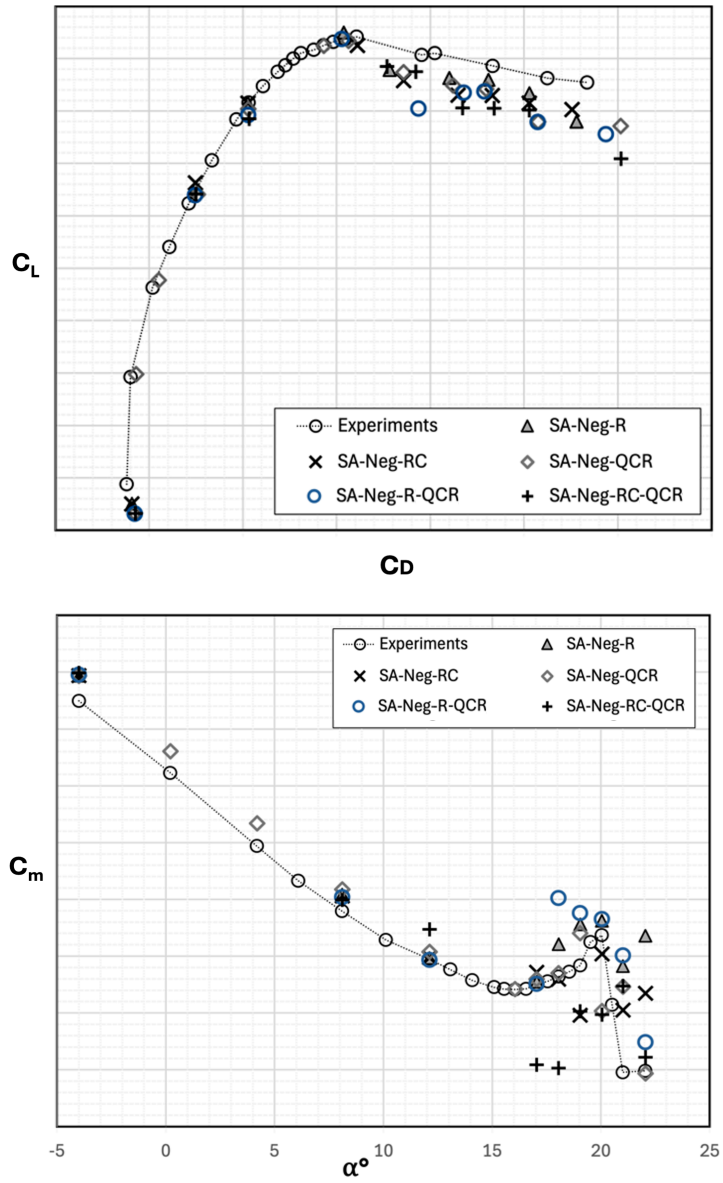

Figure 12. Comparison of the drag-polar and pitching moment (C_m).

C. Instantaneous Pressure Coefficient (C_p) – Wing and Flap

Instantaneous C_p plots for the main wing and flap are compared at various normalized spanwise locations (η) shown in Figure 13-18 against experimental data. From Figure 10 it may be deduced that there are oscillations in the flow field which indicates some time-dependency on surface pressure distribution. Multiple investigations were performed to evaluate time-sensitivity by comparing C_p development over 1 CTU. Results indicated no noticeable change suggesting that the instantaneous C_p discussed and presented in this section is a suitable analog to the averaged C_p.

Throughout the range of angles of attack investigated in this study, the effects of the Krueger flap and nacelle are noticeable (the nacelle centerline is at η ~ 0.20). Locations η = 0.24 and η = 0.37 are the two stations susceptible to nacelle wake effects. At high angles of attack, all SA model variants have a tendency to predict a nacelle induced separation which results in a significantly different pressure distribution when compared to experimental data.

For α = -4° shown in Fig.13, all the turbulence models fail to predict the correct leading-edge pressures on the main wing and the trailing-edge flaps. This disagreement is the largest at η = 0.24 and 0.37 with some improvements

for η = 0.55. At η = 0.88, once again the peak pressure at the leading-edge of the wing is significantly underpredicted. Overall, for this angle of attack, all the turbulence models struggle to predict accurate leading-edge pressures which is likely due to the presence of the Krueger flaps and nacelle wake effects.

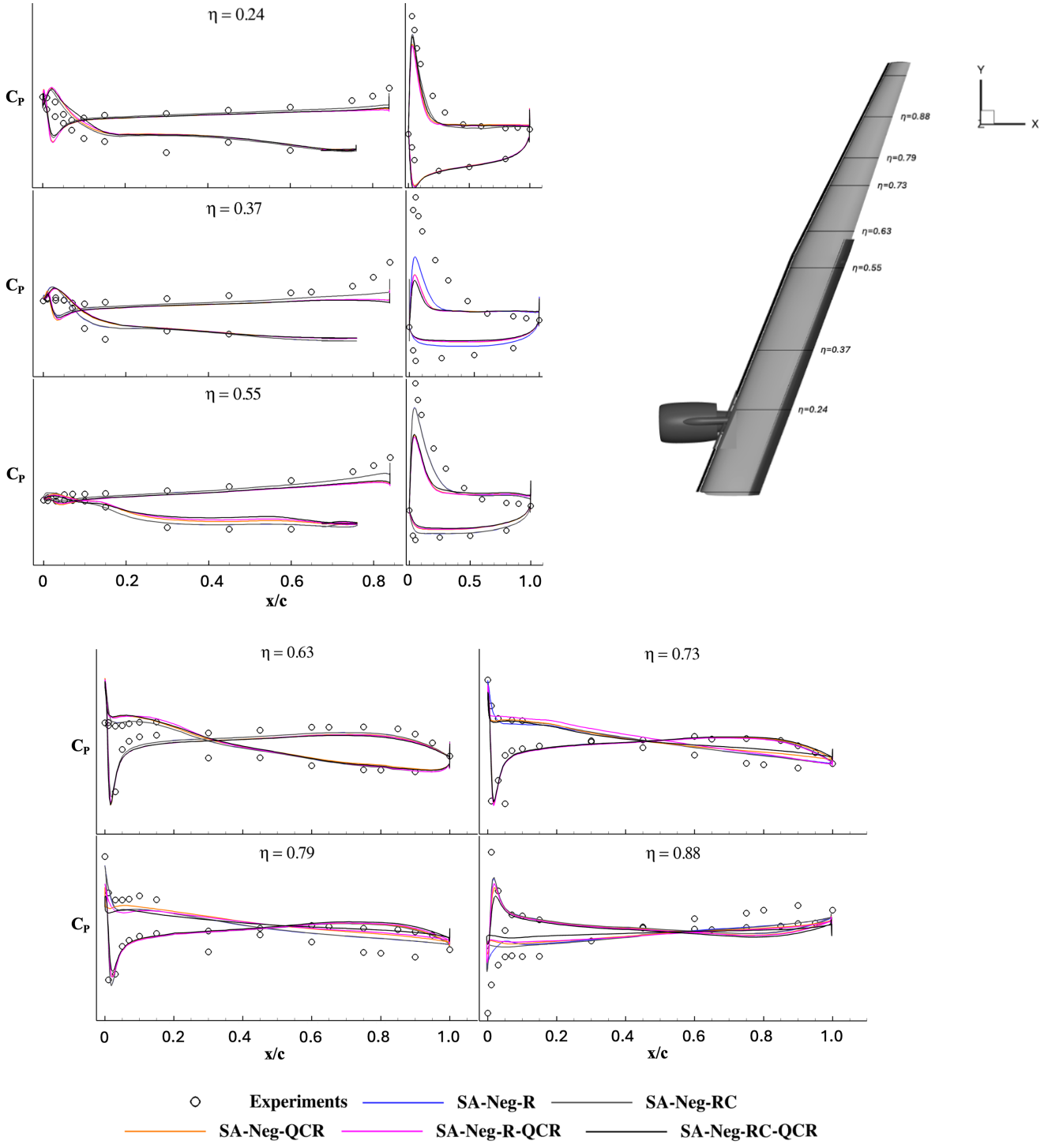

Figure 13. Pressure Coefficient at different spanwise locations (η) on the wing and flap for α = -4°.

For $\alpha = 8°$ shown in Fig.14, model predictions are consistent with experimental results. At the flap section cut at $\eta = 0.24$, experimental data show fully separated flow, while all the models except the SA-Neg-RC predict attached leading edge followed by a gradual increase in C_p. At $\eta = 0.79$, the SA-Neg-QCR model predictions are affected by the presence of a small separation zone in the vicinity of this section cut. This influences a sudden change in the local pressure distribution between $\eta = 0.79$ and $\eta = 0.88$ leading to the inaccurate prediction of C_p.

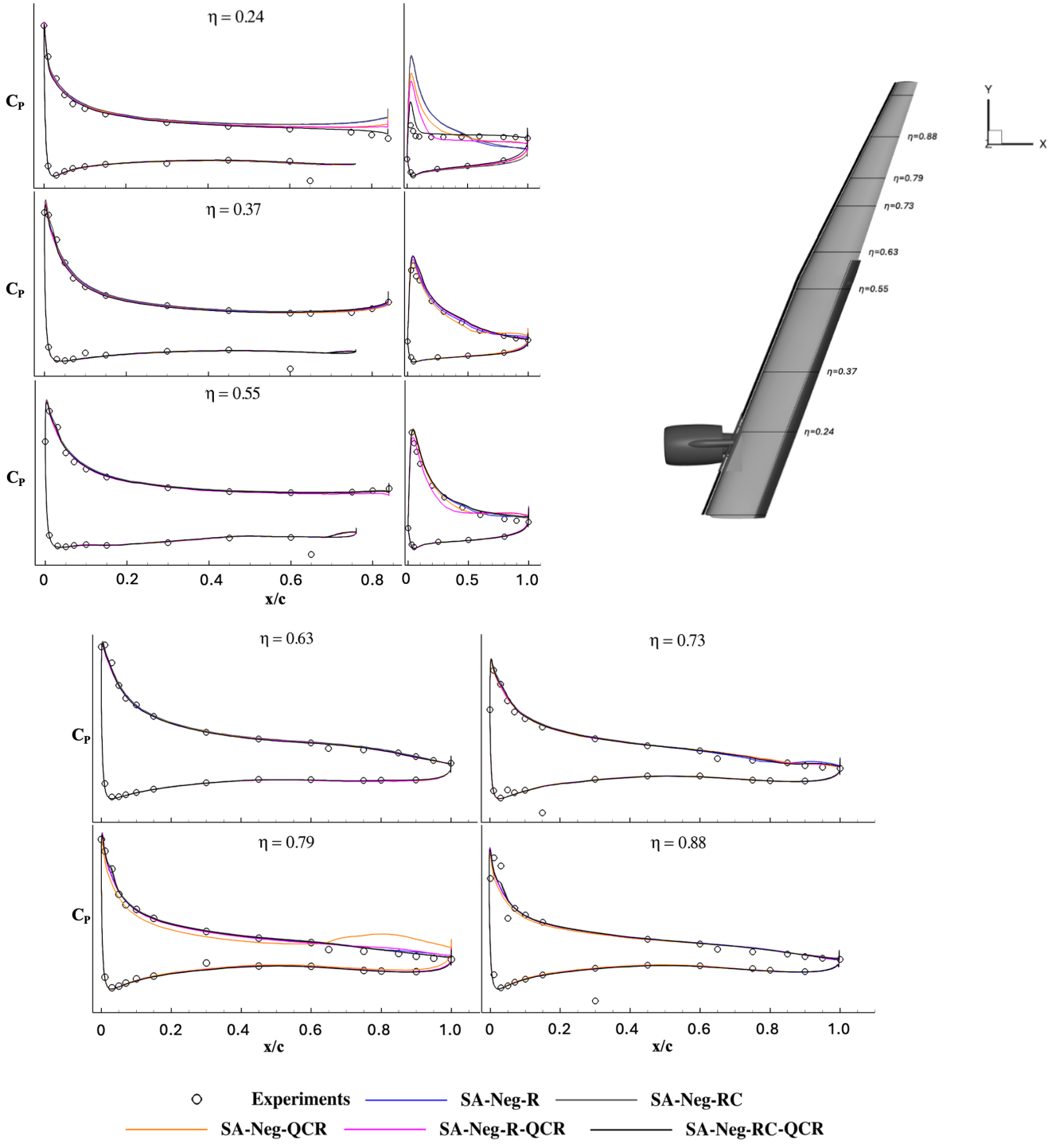

Figure 14. Pressure Coefficient at different spanwise locations (η) on the wing and flap for $\alpha = 8°$.

For $\alpha = 12°$ shown in Fig.15, once again, all the models are in relative agreement with experimental data. Interestingly, SA-Neg-RC-QCR model predicts a separated flap at $\eta = 0.37$. On the main wing for at $\eta \geq 0.73$, some disagreements between the experimental data and the simulations are observed. The major differences are caused by the simulations predicting low skin friction (discussed in the following section) zones which grow into regions of fully separated flow as the angle of attack is further increased.

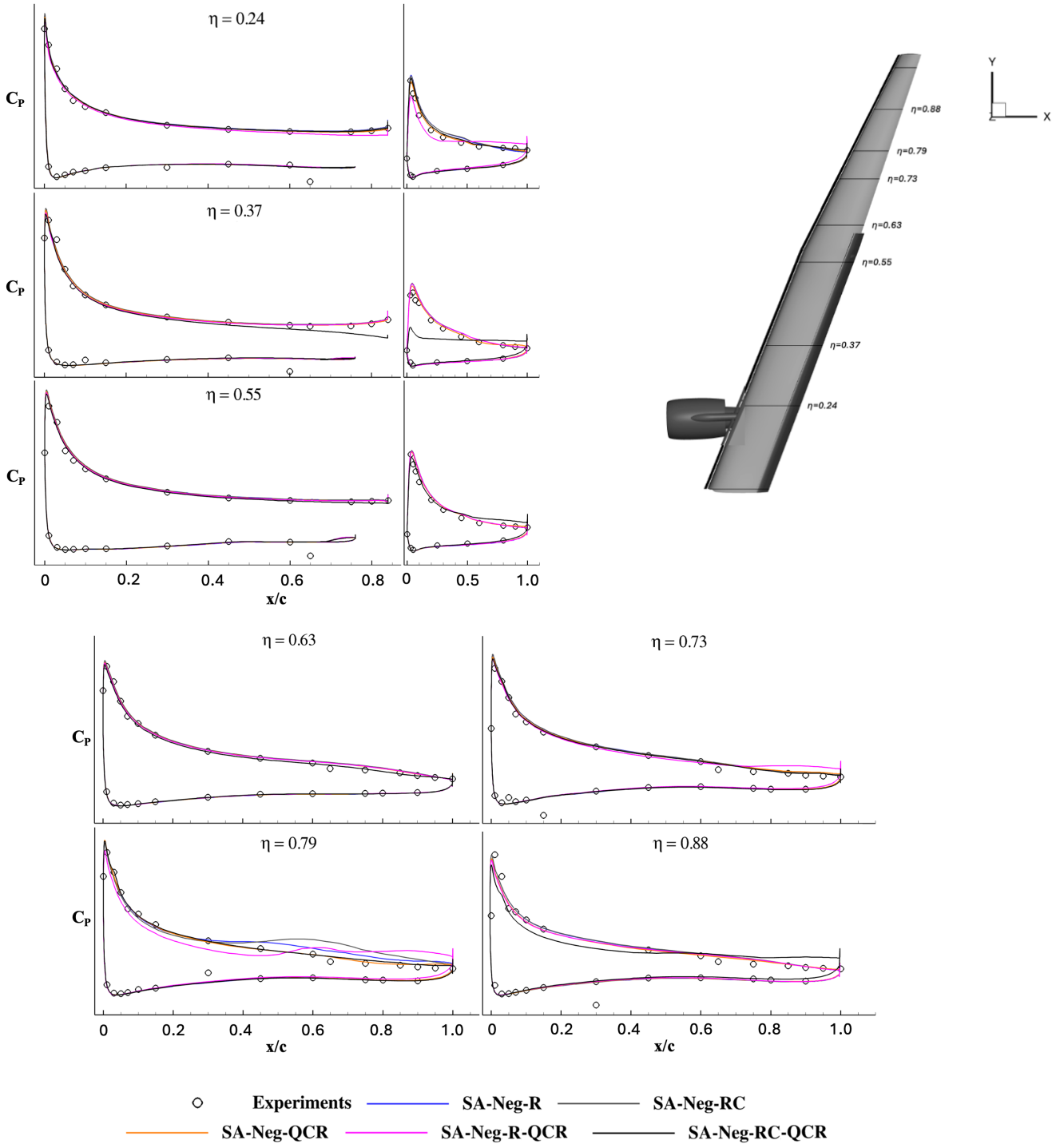

Figure 15. Pressure Coefficient at different spanwise locations (η) on the wing and flap for $\alpha = 12°$.

From Fig.11, at $\alpha = 18°$ all the turbulence models predict stall, whereas the experimental data show delayed stall until $\alpha = 19.5°$. The cause of early stall is most likely due to incorrect stress-prediction which manifests itself as a reduction in pressure leading to early separation. From Fig.16 (shown below), at $\eta = 0.24$, the SA-Neg-QCR model predicts separation, while all the other models predict attached flow. At $\eta = 0.37$, the SA-Neg-R and the SA-Neg-R-QCR models predict separation. This is the same separation bubble predicted by the SA-Neg-QCR at $\eta = 0.24$ except that in this case, it is slightly shifted in the spanwise direction.

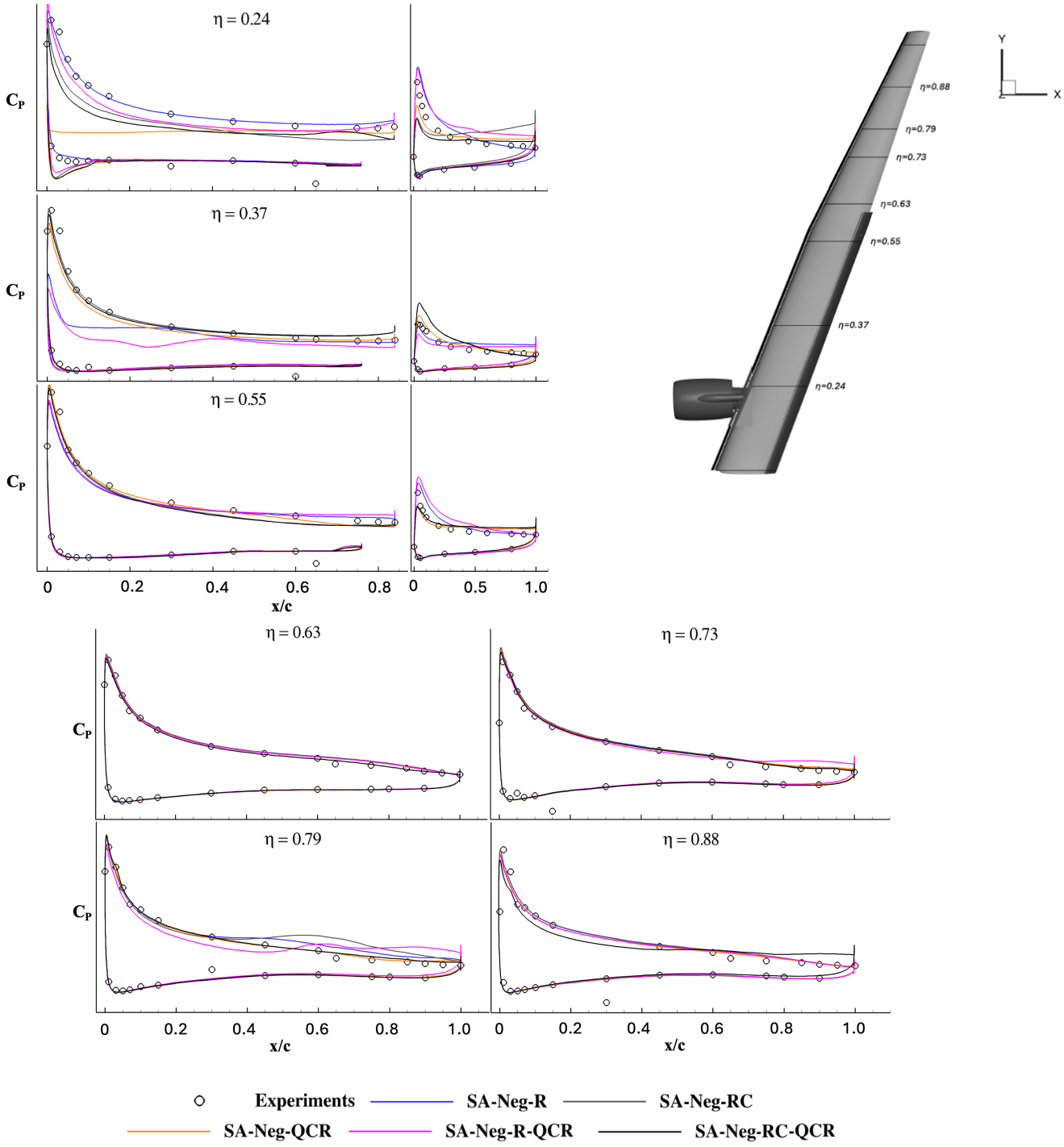

Figure 16. Pressure Coefficient at different spanwise locations (η) on the wing and flap for $\alpha = 18°$.

At $\alpha = 20°$ shown in Fig.17, all the models are affected by the wake of the nacelle for $\eta = 0.24$ and $\eta = 0.37$ locations. Based on the location of the separated region caused by the nacelle, the models alternate between an attached leading edge with gradual change in C_p and an attached leading edge followed by a region of separated flow. However, the flap pressures in these locations are more consistently predicted. On the outboard side, all the models predicted a fully attached wing at $\eta = 0.73$, while experimental data suggests a region of flow separation. This is primarily due to the prediction of separated flow zones that differ in size, shape, and location as predicted by each turbulence model.

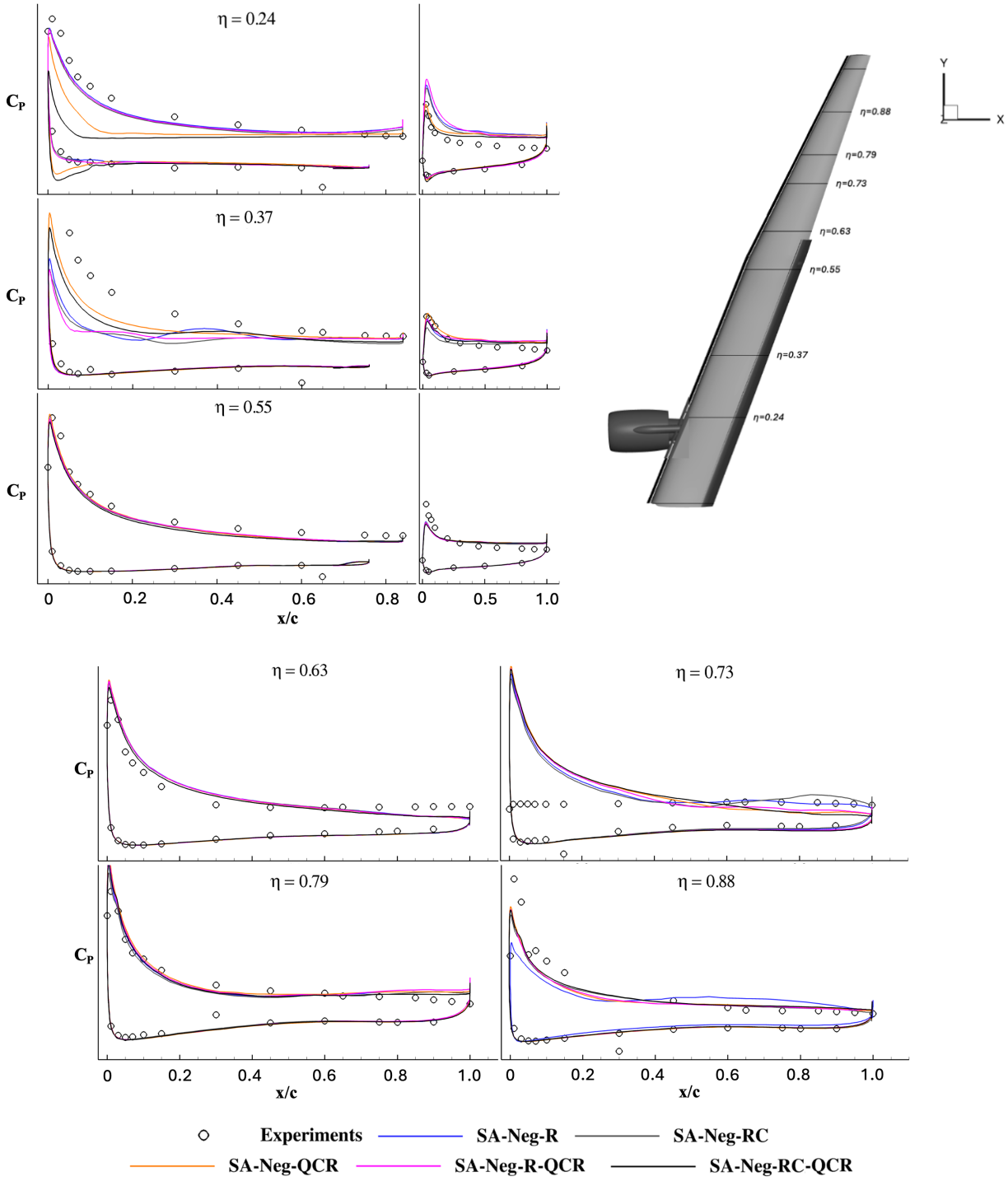

Figure 17. Pressure Coefficient at different spanwise locations (η) on the wing and flap for $\alpha = 20°$.

Finally, at α = 22° shown in Fig.18, large areas of separated flow zones appear on the wing surface (discussed in the following section). Although all the models capture the flap pressures with relatively high accuracy, major disagreements between the experiment and simulation results are observed for the main wing pressure distributions. Similar to the C_p distribution at α = 20°, the size and location of the separated flow zones vary significantly. Overall, only qualitative agreement between the simulation and the experiment is achieved. Also, predictions for α = 20° and 22° highlight the failure of industry standard RANS models to accurately predict flow associated with a stalled wing.

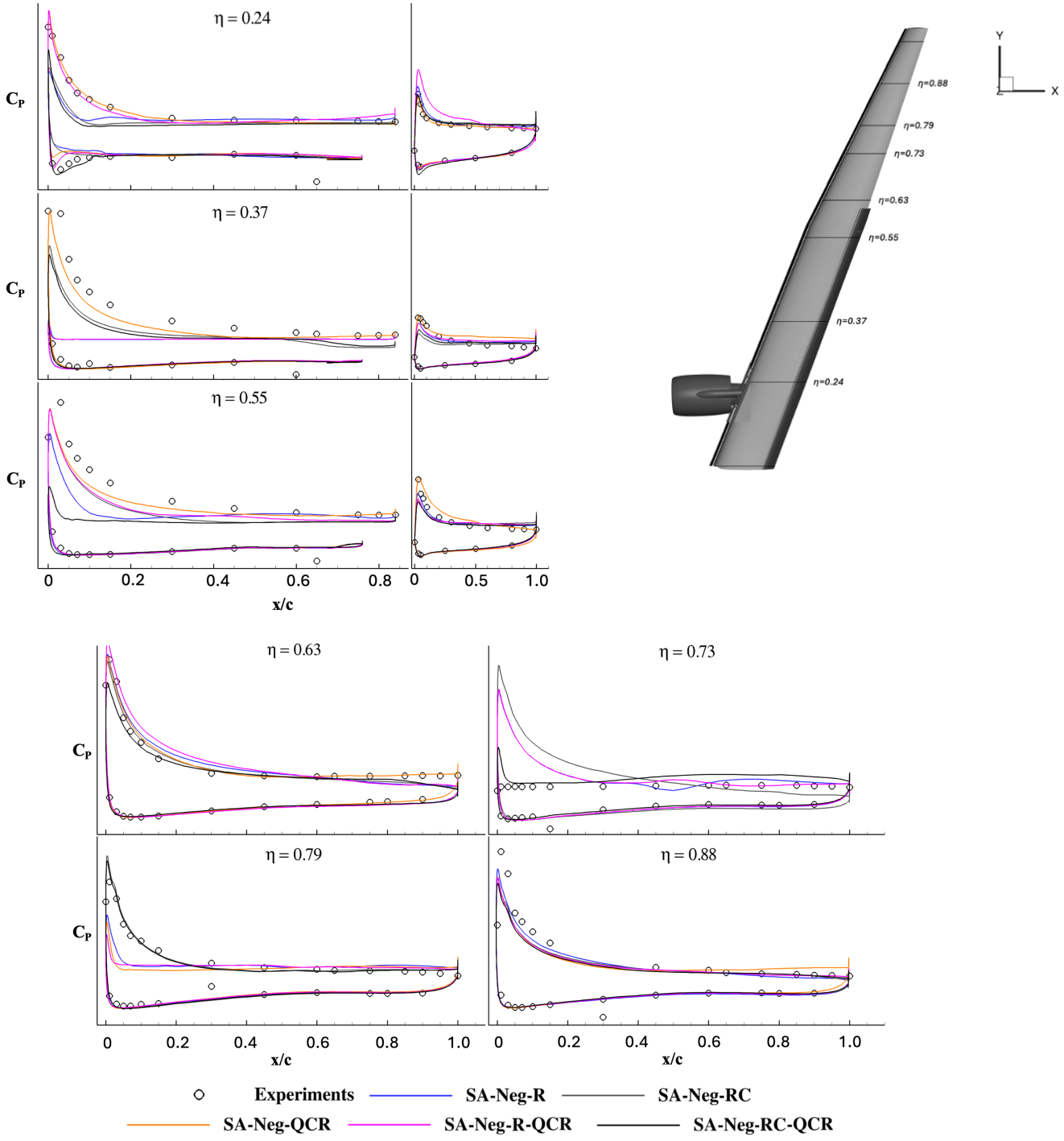

Figure 18. Pressure Coefficient at different spanwise locations (η) on the wing and flap for α = 22°.

D. Instantaneous normalized Skin Friction Coefficient (C_f) Magnitude

Contours of normalized skin friction coefficient (C_f) magnitude are generated and shown in Figs. 19-24 for α = -4°, 8°, 12°,18°, 20°, and 22°. A consistent feature on high-lift systems is the presence of low C_f streaks, which are a result of leading-edge control surfaces such as Krueger flap brackets. At α = -4° shown in Fig.19, all the models predict a separated leading-edge for $\eta \leq 0.55$ due to the presence of the Krueger and nacelle. The flap is also predicted to be separated. At α = 8° (see Fig.20), streaks of low skin friction zones appear as the flow interacts with the Krueger brackets. Interestingly, the SA-Neg-QCR model predicts the presence of a separated wedge or 'pizza slice' between $0.79 < \eta < 0.88$. At α = 12° (see Fig.21), all the models predict the presence of 'pizza slices' in the outboard sections of the wing. At α = 18° (see Fig.22), large patches of separated flow appear on the inboard side of the wing as the nacelle ($\eta \sim 0.20$) wakes create regions of separated flow. These separated zones either appear at $\eta < 0.24$ for the rotation corrected (SA-Neg-R and SA-Neg-R-QCR) model variants or at $\eta \sim 0.37$ for the other models. Interestingly, the baseline SA-Neg-QCR model predicts the largest separation bubble at η = 0.24. Further increase in angle of attack to α = 20° (see Fig.23) stalls the wing and large regions of separated flow appear on the inboard and outboard sections of the wing. Finally, at α = 22° (see Fig.24), all the models predict large regions of flow separation with the SA-Neg-RC model predicting a relatively cleaner mid-wing section leading to improved lift.

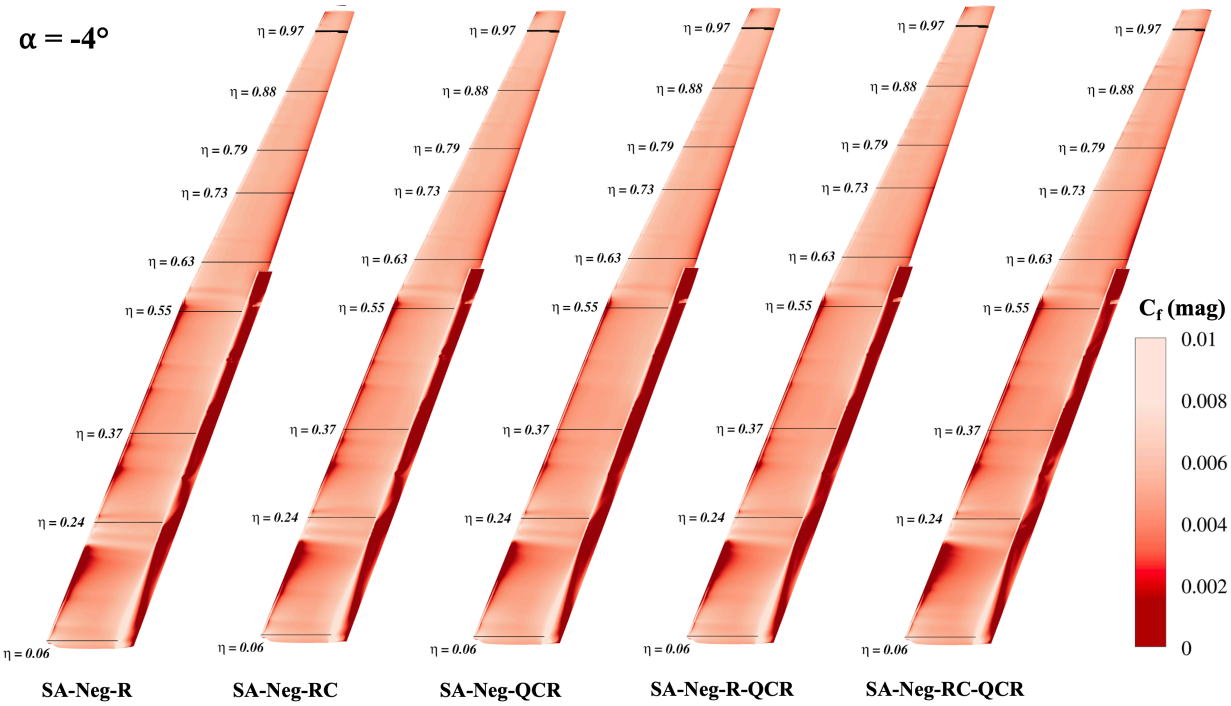

Figure 19. Contours of instantaneous normalized skin-friction magnitude on the wing (suction-side) at α= -4°.

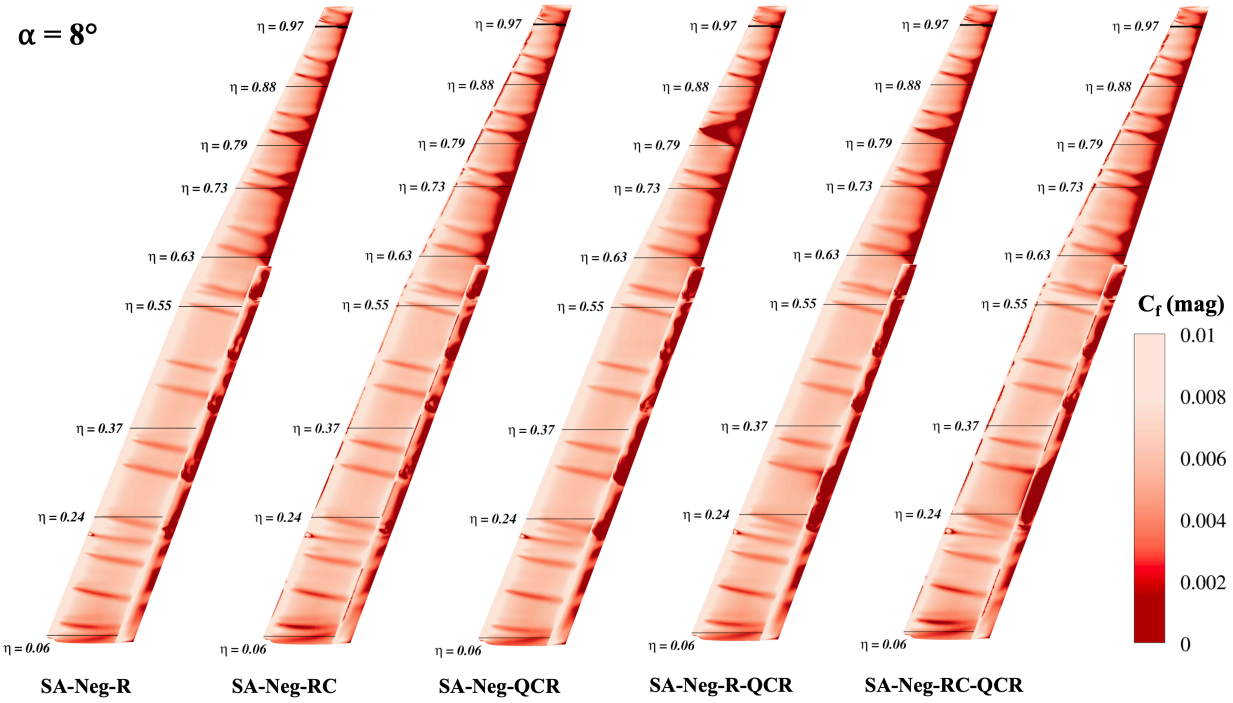

Figure 20. Contours of instantaneous normalized skin-friction on the wing (suction-side) at α= 8°.

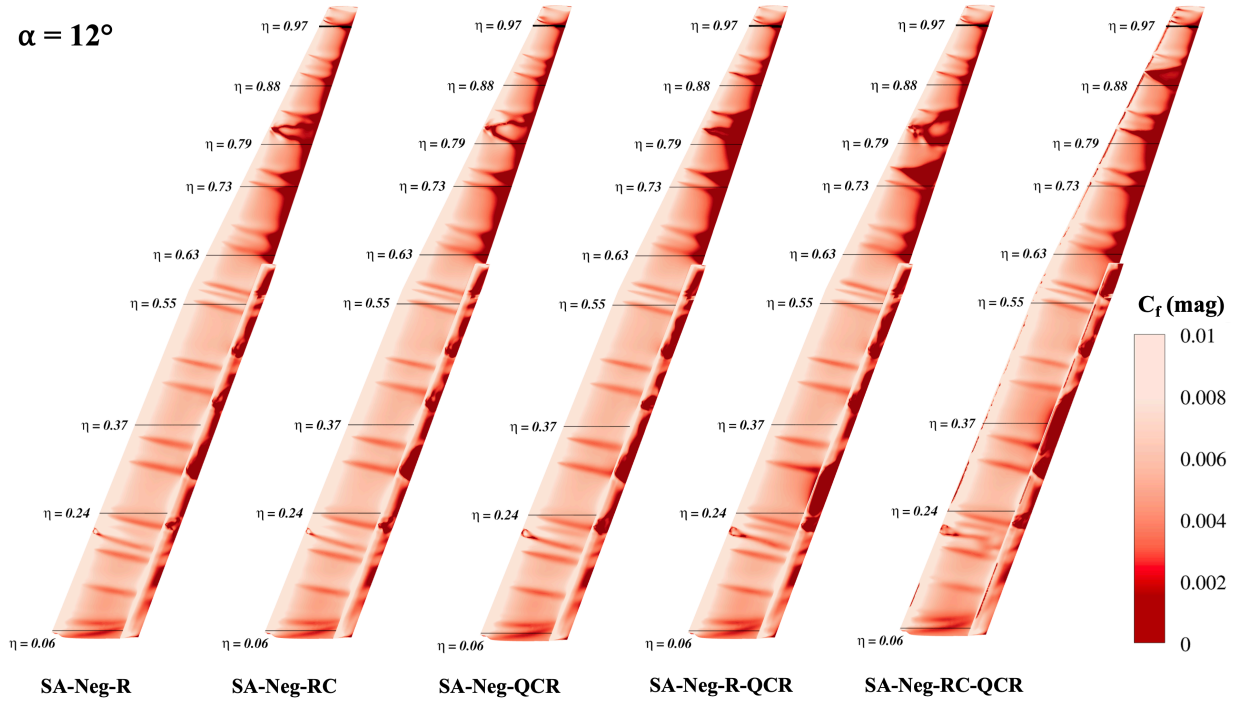

Figure 21. Contours of instantaneous normalized skin-friction magnitude on the wing (suction-side) at α= 12°.

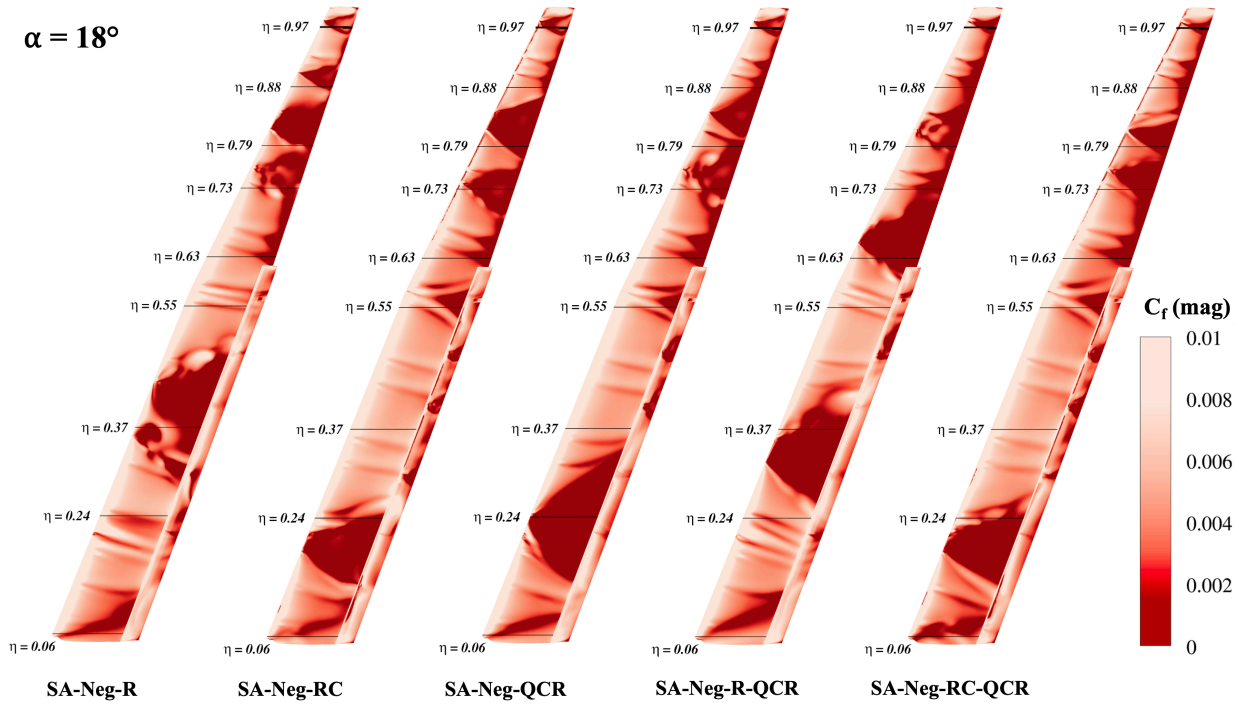

Figure 22. Contours of instantaneous normalized skin-friction magnitude on the wing (suction-side) at α= 18°.

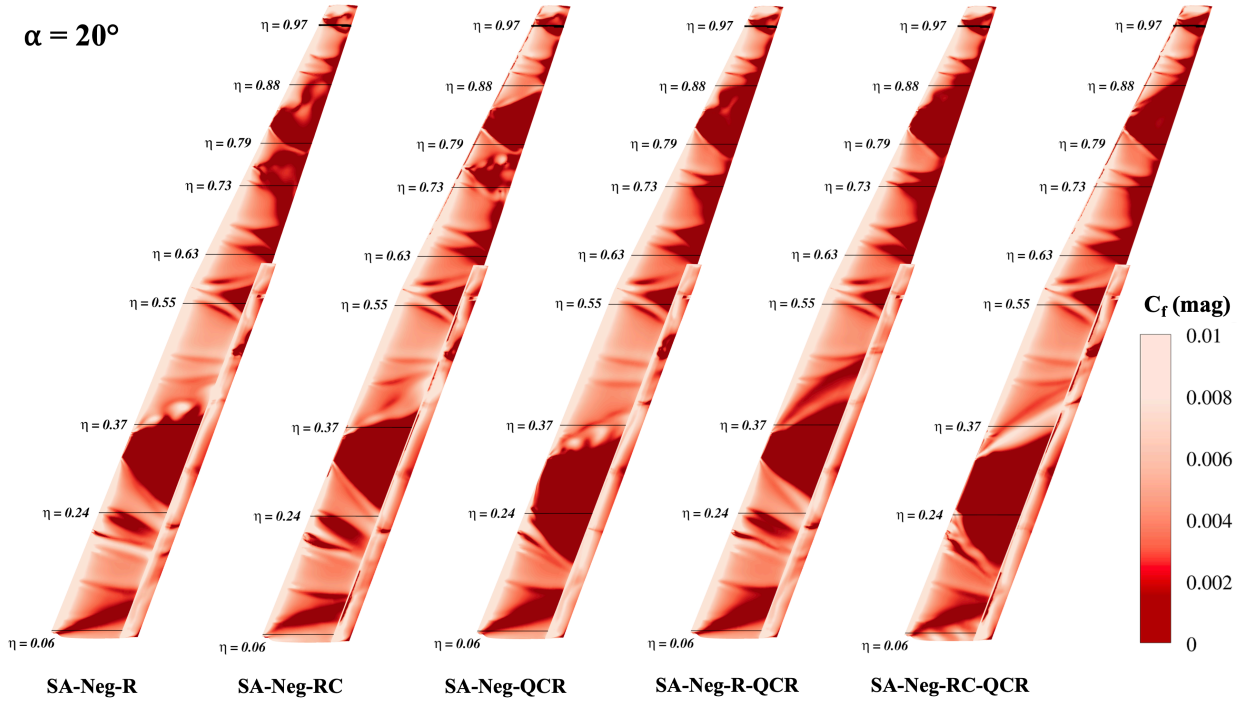

Figure 23. Contours of instantaneous normalized skin-friction magnitude on the wing (suction-side) at α= 20°.

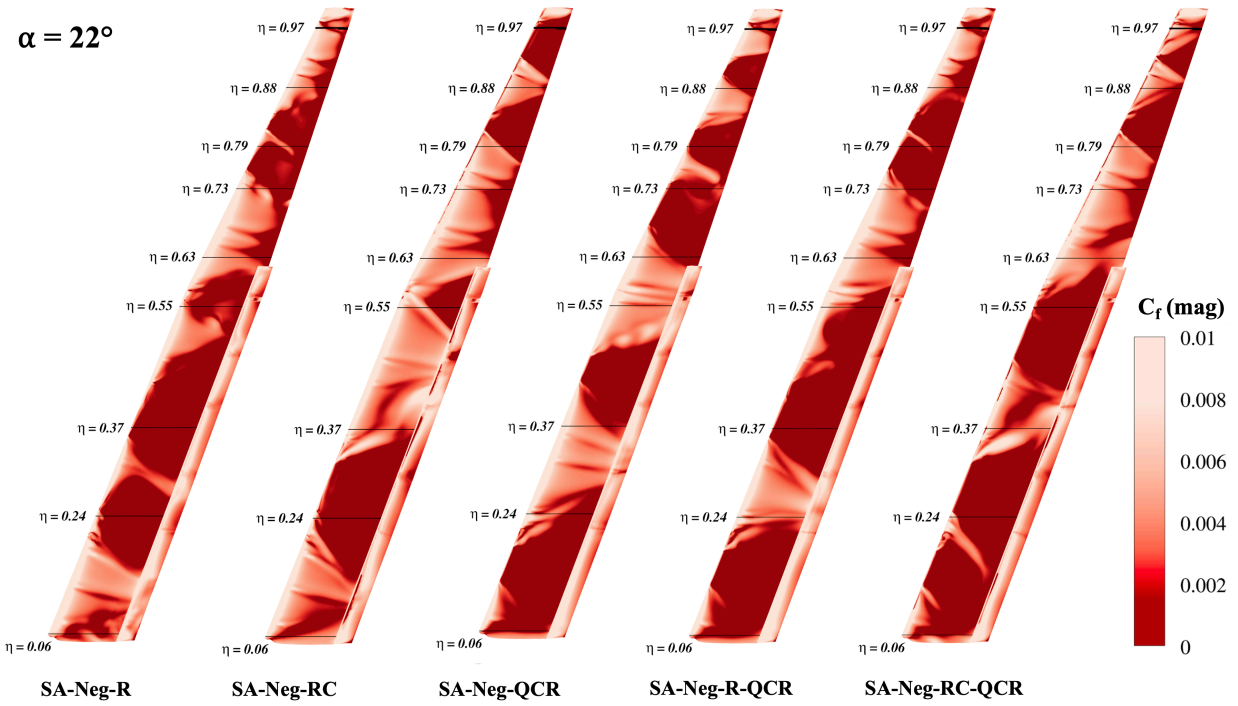

Figure 24. Contours of instantaneous normalized skin-friction magnitude on the wing (suction-side) at α= 22°.

VIII. Conclusions

Time-accurate numerical simulations of the SUGAR TTBW high-lift configuration are carried out using USM3D-ME solver for α = -4° to 22° at M_∞ = 0.20 using SA-Neg-R, SA-Neg-RC, SA-Neg-QCR, SA-Neg-R-QCR and SA-Neg-RC-QCR turbulence models. Results indicate that all the models are in relatively good agreement with experimental observations in the linear region of the lift-curve except for α = -4°. The models also predict features, such as lift-break, relatively accurately, which are sometimes challenging for RANS models. However, all models inaccurately predict early stall followed by a significant loss in lift. In this region, pitching moment predictions vary significantly. Although the pitch-break behavior is predicted relatively well, near-stall, all the models predict pitching moments with varying degrees of disagreement against the experiment. The SA-Neg-R and SA-Neg-RC perform relatively well when compared to their QCR counterparts. The major reason for the early stall and lack of consistent pitching moment predictions are attributed to the presence of large, separated wedges also known as 'pizza slices' that initially dominate the outboard side of the wing around stall. At post-stall angles, large, separated flow caused by the nacelle dominates the inboard side as highlighted in Figs. 19-23. This behavior of RANS models highlights the importance of predicting accurate stresses in the pre-boundary layer separation region as well as the separated shear layer. It is likely that underprediction of stresses for post-stall angles-of-attack are responsible for the tendency of the SA family of models to underpredict lift. This aligns with the relative improvements in hybrid RANS-LES model predictions in these regions where resolved stresses tend to dominate the flow field enabling HRL models to make improved predictions.

Overall, it is concluded that although URANS models are able to predict the aerodynamic behavior of high-lift configurations with relative accuracy, due to the complexities associated with separated flows at high angles of attack, the use of scale-resolving simulations such as hybrid RANS-LES models should be considered.

IX. Future Work

Future work associated with the Mach 0.80 SUGAR configuration of Transonic Truss-Braced Wing configuration will include high fidelity simulations using Hybrid RANS-LES [27-30] using USM3D-ME. Current work is ongoing which focuses on a new production term for the SA model that promotes reattachment based on local flow statistics. Initial results for CRM-HL have shown an improvement in integrated forces and pitching moments. Future publications will be dedicated to the new turbulence model and its application for high-lift configurations. Additional

numerical strategies for solving this type of unsteady flow currently under development within the USM3D-ME framework include Wall-Modeled LES, non-stationary time-filtering [49,50], Algebraic Reynolds-Stress Models, and optimization of the solver for use on Graphics Processing Units.

Acknowledgments

This research has been funded by NASA Advanced Air Transport Technology (AATT) Project. Computer resources were provided by the NASA Advanced Supercomputing (NAS) facility under the High-End Computing Capability (HECC) Project.

References

[1] Rumsey, C.L., Slotnick, J.P., and Sclafani, A.J., "Overview and Summary of the Third AIAA High Lift Prediction Workshop", Journal of Aircraft, 2019, 56:2, 621-644.

[2] Rumsey, C.L., Slotnick, J. P., Long, M., Stuever, R.A., and Wayman, T. R., "Summary of the First AIAA CFD High-Lift Prediction Workshop", Journal of Aircraft, 2011, 48:6, 2068-2079.

[3] Pomeroy, B.W., Ansell, P.J., Diebold, J.M., and Selig, M.S., "A Study of Burst Wakes in a Multielement Airfoil Flowfield," AIAA 2013-2919, 31st AIAA Applied Aerodynamics Conference, June 2013.

[4] Pandya, M.J., Abdol-hamid, K., and Parlette, E., "CFD Computations for a Generic High-Lift Configuration Using TetrUSS," AIAA 2011-3008, 29th AIAA Applied Aerodynamics Conference, June 2011.

[5] Spalart, P.R., and Allmaras, S. A., "One-Equation Turbulence Model for Aerodynamic Flows," AIAA Paper 92-0439, January 1992.

[6] Menter, F.R., "Improved Two-Equation k-omega Turbulence Models for Aerodynamic Flows," NASA TM-103975, October 1992.

[7] Frink, N. T., Pirzadeh, S. Z., Parikh, P. C., Pandya, M. J., and Bhat, M. K., "The NASA tetrahedral unstructured software system (TetrUSS)," The Aeronautical Journal, Vol. 104, No. 1040, 2000, pp. 491-499.

[8] Pandya, M. J., Frink, N. T., Abdol-Hamid, K. S., Samareh, J. A., and Taft, J. R., "Enhancements to TetrUSS for NASA Constellation Program," AIAA Paper 2011-1111.

[9] Abdol-Hamid, K. S., Frink, N. T., Deere, K. A., and Pandya, M. J., "Propulsion Simulations Using Advanced Turbulence Models with the Unstructured-Grid CFD Tool, TetrUSS," AIAA Paper 2004-0714, January 2004.

[10] Pandya, M.J., Frink, N.T., and Noack, R.W., "Overset-grid moving body capability in the USM3D unstructured flow solver," AIAA Paper 2005-5118.

[11] Lacy, D. S. and Sclafani, A. J., "Development of the High Lift Common Research Model (HL-CRM): A Representative High Lift Configuration for Transonic Transports", 54th AIAA Aerospace Sciences Meeting, AIAA Paper 2016-0308, San Diego, CA, Jan. 2016

[12] Coder, J.G., Pulliam, T.H., and Jensen, J.C., "Contributions to HiLiftPW-3 Using Structured, Overset Grid Methods," AIAA 2018-1039. 2018 AIAA Aerospace Sciences Meeting. January 2018.

[13] Spalart, P. R., "Strategies for Turbulence Modelling and Simulation," International Journal of Heat and Fluid Flow, Vol. 21, 2000, pp. 252–263.

[14] Bozeman, M.D., and Pandya, M.J., "Mixed-element USM3D Contributions to the 4th AIAA High Lift Prediction Workshop," AIAA 2023-1759. AIAA SCITECH 2023 Forum. January 2023.

[15] Pandya, M. J., Frink, N. T., Ding, E., and Parlette, E. B., "Toward Verification of USM3D Extensions for Mixed Element Grids," AIAA Paper 2013-2541, 31st Applied Aerodynamics Conference, San Diego, CA, June 2013; DOI: 10.2514/6.2013-2541

[16] Pandya, M. J., Diskin B., Thomas, J. L., and Frink N. T., "Improved Convergence and Robustness of USM3D Solutions on Mixed Element Grids," AIAA Journal (2016), 54(9), pp. 2589-2610; DOI: 10.2514/1.J054545

[17] Pandya, M. J., Diskin B., Thomas, J. L., and Frink N. T., "Assessment of USM3D Hierarchical Adaptive Nonlinear Method Preconditioners for Three-Dimensional Cases," AIAA Journal (2017) 55(10), pp. 3409-3424; DOI:10.2514/1.J055823

[18] Pandya, M. J., Jespersen, D. C., Diskin B., Thomas, J. L., and Frink, N. T., "Efficiency of Mixed-Element USM3D for Benchmark Three-Dimensional Flows," AIAA Journal (2021), 59(8), pp. 2997-3011; DOI: 10.2514/1.J059720

[19] Pandya M. J., Jespersen, D. C., Diskin B., Thomas, J. L., and Frink, N. T., "Verification and Scalability of Mixed-Element USM3D for Benchmark Three-Dimensional Flows," AIAA Journal (2021), 59(11), pp. 4719-4738; DOI: 10.2514/1.J060064

[20] Allmaras, S. R., Johnson, F. T., and Spalart, P. R., "Modifications and Clarifications for the Implementation of the Spalart-Allmaras Turbulence Model," ICCFD7-1902, 7th International Conference on Computational Fluid Dynamics, Big Island, Hawaii, 9-13 July 2012
[21] Shur, M.L., Strelets, M.K., Travin, A.K., and Spalart, P.R., "Turbulence Modeling in Rotating and Curved Channels: Assessing the Spalart-Shur Correction", AIAA Journal 2000 38:5, 784-792
[22] Lacy, D. S., and Clark, A. M., "Definition of Initial Landing and Takeoff Reference Configurations for the High Lift Common Research Model (CRM-HL)," AIAA AVIATION 2020 FORUM, 2020, p. 2771.
[23] Harrison, N.A., Hoffman, K., Lazzara, D.S., Reichenbach, E.Y., Sclafani, A.J., and Droney, C.K., "Subsonic Ultra Green Aircraft Research: Phase IV Final Report–Volume I Mach 0.80 Transonic Truss-Braced Wing High-Speed Design Report," 2023.
[24] Maldonado, D., Viken, S.A., Housman, J.A., Hunter, C.A., Duensing, J.C., Frink, N.T., Jensen, J.C., McMillin, S.N., and Kiris, C.C., "Computational Simulations of a Mach 0.745 Transonic Truss-Braced Wing Design," AIAA 2020-1649. AIAA Scitech 2020 Forum. January 2020.
[25] Kiris, C.C, Housman, J., Barad, M., Brehm, C., Sozer, E., and Moini-Yekta, S., "Computational Framework for Launch, Ascent, and Vehicle Aerodynamics (LAVA)," Aerospace Science and Technology, Vol. 55, 2016, pp. 189–219.
[26] Viken, S.A., Hunter, C.A., McMillin, S.N., Gatlin, G.M., Maldonado, D., Housman, J.A., Duensing, J.C., Jensen, J.C., and Kiris, C.C.," Comparison of Computational Predictions of the Mach 0.80 Transonic Truss-Braced Wing Configuration with Experimental Data," Tech. rep., 2022.
[27] Spalart, P., Jou, W-H., Strelets, M., and Allmaras, S., 1997, "Comments on the Feasibility of LES for Wings, and on a Hybrid RANS/LES Approach," Advances in DNS/LES: First AFOSR International Conference on DNS/LES, C. Liu and Z. Liu, eds. (Greyden, Columbus, OH).
[28] Spalart, P. R., Deck, S., Shur, M. L., Squires, K. D., Strelets, M. K., & Travin, A. (2006). A New Version of Detached-eddy Simulation, Resistant to Ambiguous Grid Densities. Theoretical and Computational Fluid Dynamics, 20(3), 181-195. doi:10.1007/s00162-006-0015-0
[29] Bhushan, S., Walters, D.K., (2012). "A Dynamic Hybrid RANS/LES Modeling Framework," Physics of Fluids 24, No. 015103.
[30] Jamal, T, Shobayo, OO, and Walters, DK. "A New Variant of the Dynamic Hybrid RANS-LES Model for Complex Turbulent Flows." Proceedings of the ASME 2021 International Mechanical Engineering Congress and Exposition. Volume 10: Fluids Engineering. Virtual, Online. November 1–5, 2021. V010T10A052. ASME. https://doi.org/10.1115/IMECE2021-72185
[31] Taylor, BH, Jamal, T, & Walters, DK. "Performance Evaluation of a Non-Linear Explicit Algebraic Reynolds Stress Model for Surface Mounted Obstacles." Proceedings of the ASME 2020 Fluids Engineering Division Summer Meeting collocated with the ASME 2020 Heat Transfer Summer Conference and the ASME 2020 18th International Conference on Nanochannels, Microchannels, and Minichannels. Volume 3: Computational Fluid Dynamics; Micro and Nano Fluid Dynamics. Virtual, Online. July 13–15, 2020. V003T05A025. ASME. https://doi.org/10.1115/FEDSM2020-20304
[32] Jamal, T, and Walters, DK. "Investigation of an Algebraic Reynolds Stress Model for Simulation of Wall-Bounded Turbulent Flows With and Without Buoyancy Effects." Proceedings of the ASME 2020 Fluids Engineering Division Summer Meeting collocated with the ASME 2020 Heat Transfer Summer Conference and the ASME 2020 18th International Conference on Nanochannels, Microchannels, and Minichannels. Volume 3: Computational Fluid Dynamics; Micro and Nano Fluid Dynamics. Virtual, Online. July 13–15, 2020. V003T05A042. ASME. https://doi.org/10.1115/FEDSM2020-20354
[33] Wallin, S., Johansson, A.V., "An explicit algebraic Reynolds Stress model for incompressible and compressible turbulent flows," J.Fluid Mech., Vol.403, Pages 89-132.
[34] Speziale, C.G., "On nonlinear K-l and K-ε models of turbulence", Journal of Fluid Mechanics. 1987; 178:459-475. doi:10.1017/S0022112087001319
[35] Kegerise, M. A., and Neuhart, D. H., "An Experimental Investigation of a Wing-Fuselage Junction Model in the NASA Langley 14- by 22-Foot Subsonic Tunnel," NASA TM-2019-220286, June 2019, https://doi.org/https://ntrs.nasa.gov/archive/nasa/casi.ntrs.nasa.gov/20190027403.pdf.
[36] Rumsey, C. L., Neuhart, D. H., and Kegerise, M. A., "The NASA Juncture Flow Experiment: Goals, Progress, and Preliminary Testing," AIAA Paper 2016-1557, Jan.2016.https://doi.org/10.2514/6.2016-1557
[37] Rumsey, C. L., "The NASA Juncture Flow Test as a Model for Effective CFD/Experimental Collaboration," AIAA Paper 2018-3319, June 2018. https://doi.org/10.2514/6.2018-3319.

[38] Mani, M., Babcock, D., Winkler, C., and Spalart, P.R., "Predictions of a Supersonic Turbulent Flow in a Square Duct," AIAA 2013-860. 51st AIAA Aerospace Sciences Meeting including the New Horizons Forum and Aerospace Exposition. January 2013.
[39] Rumsey, C.L., Carlson, J.R., Pulliam, T.H., and Spalart, P.R., "Improvements to the Quadratic Constitutive Relation Based on NASA Juncture Flow Data," AIAA Journal 2020 58:10, 4374-4384
[40] Rodi, W. (1976), A New Algebraic Relation for Calculating the Reynolds Stresses. Z. Angew. Math. Mech., 56: T219-T221. https://doi.org/10.1002/zamm.19765613093
[41] Rumsey, C.L., and Gatski, T.B., "Recent Turbulence Model Advances Applied to Multielement Airfoil Computations," Journal of Aircraft 2001 38:5, 904-910
[42] Rumsey, C., and Gatski, T., "Summary of EASM Turbulence models in CFL3D with validation test cases", Tech. rep., 2003.
[43] Hellsten, A., "New Advanced k-w Turbulence Model for High-Lift Aerodynamics," AIAA Journal 2005 43:9, 1857-1869
[44] Dacles-Mariani, J., Kwak, D., and Zilliac, G., "On numerical errors and turbulence modeling in tip vortex flow prediction," International journal for numerical methods in fluids 30.1 (1999): 65-82.
[45] Dacles-Mariani, J., Zilliac, G.G., Chow, J.S., and Bradshaw, P., "Numerical/experimental study of a wingtip vortex in the near field," AIAA journal 33.9 (1995): 1561-1568.
[46] NASA, "14- by 22-Foot Subsonic Tunnel," 2024. URL https://www.nasa.gov/directorates/armd/14-by-22-foot-subsonic-tunnel/
[47] Dickey, E.D., Straccia, J.C., Harrison, N. A., Patel, D., and Malone, A. M., "Subsonic Ultra Green Aircraft Research: Phase V Final Report – Transonic Truss-Braced Wing High-Lift Test #2", NASA/CR–2022-000000, 2022.
[48] Wick, A., and Hooker, R., HeldenMesh User's Manual Version *3.05*, Helden Aerospace Corporation, June 2018.
[49] Jamal, T, & Walters, DK. "A Dynamic Time Filtering Technique for Hybrid RANS-LES Simulation of Non-Stationary Turbulent Flow." Proceedings of the ASME-JSME-KSME 2019 8th Joint Fluids Engineering Conference. Volume 2: Computational Fluid Dynamics. San Francisco, California, USA. July 28–August 1, 2019. V002T02A051. ASME. https://doi.org/10.1115/AJKFluids2019-4696
[50] Jamal, T., Shobayo, O., Walters, D. K., and Bhushan, S. (March 14, 2025). "Static and Dynamic Time Filtering Techniques for Hybrid RANS-Large Eddy Simulation of Non-Stationary Turbulent Flows." ASME. *J. Fluids Eng*. August 2025; 147(8): 081502. https://doi.org/10.1115/1.4067790